2022-05-09

Development of an Experimental Platform to Enable Ultrasound Neuromodulation Studies

Loree-Spacek, Jak

UNIVERSITY OF CALGARY

Development of an Experimental Platform to Enable Ultrasound Neuromodulation Studies

by

Jak Loree-Spacek

A THESIS

SUBMITTED TO THE FACULTY OF GRADUATE STUDIES

IN PARTIAL FULFILMENT OF THE REQUIREMENTS FOR THE

DEGREE OF MASTER OF SCIENCE

GRADUATE PROGRAM IN BIOMEDICAL ENGINEERING

CALGARY, ALBERTA

MAY, 2022

Abstract

Focused ultrasound (FUS) neuromodulation is the delivery of concentrated mechanical energy into central nervous tissue at low intensity (a few W per cm^2; about as intense as imaging ultrasound, and not sufficiently intense to cause heating) with the goal of eliciting a functional change. It is of interest to applied and clinical scientists as a prospective non-invasive therapeutic intervention; it is also applicable to basic scientists as a tool for *in vivo* brain mapping. This work details the development of a device and accompanying system that enables the study of ultrasound-mediated neuromodulation in brain tissue samples in a setting with concurrent electrophysiology. We use a novel ultrasound focusing technique based on principles of acoustic reflection, and the first research chapter discusses the development and integration of this focusing technique. To develop and refine our design, I used finite-element modeling and iterative computer optimization techniques. The concordance of these *in silico* techniques with reality was verified with prototypes and hydrophone acoustic field measurements. Subsequently, several production-quality ultrasound units were produced to the specifications determined by modeling; these units exhibited performance improvements based on the results from testing prototypes, and they were characterized in terms of efficiency, electrical impedance, and ultrasonic pressure field shape. We used two independent methods to verify the absolute acoustic intensity output by our device: radiation-force absorber measurements in conjunction with wide-field hydrophone scans, and then later a calibrated hydrophone. The second research chapter of this manuscript describes the application of our system to neuroscientific experiments: I detail how we obtained early data pertaining to the ability of pulsed FUS to modulate field potential activity in acute animal brain slices. We observed an intensity-dependent modulation effect in a majority of slices tested (>50%, n=44); however, this effect was determined to be dominated by a confound and unlikely to be physiological. This course of study explored and evaluated a novel technique for obtaining an ultrasound focus; it also yielded a system that enables further experiments into interactions between FUS and brain tissue. This manuscript, the devices resulting from the work, and the documentation included in the appendices will enable continued investigations into ultrasound neuromodulation at the University of Calgary.

Preface

The introductory chapter of this document includes material reproduced from my research proposal "Design and Construction of Novel Devices for Ultrasound Neuromodulation Experiments," submitted to my committee July 19, 2019. Re-used material includes Figure 1 and various wordings.

Chapter 2 ("Development of a Computer-Optimized Experiment Platform for Neuromodulation Studies") of this thesis includes data and results previously published in J. Loree-Spacek, C. Swytink-Binnema, Z. Kiss, L. Curiel, and S. Pichardo, "Fabrication and Validation of an Acoustic Reflective Casing for Neurostimulation Studies with Microscopy," in the proceedings of the 2020 IEEE International Ultrasonics Symposium (September 2020). Figure 9 is re-used from the same.

Chapter 3 ("Replicability Study: Ultrasound-Induced Modulation of *in vitro* Evoked Local Field Potentials") of this thesis is original work that has not been submitted for publication, but it is adapted from "Application of an Acoustic Reflective Casing for *in vitro* Neuromodulation: Pilot Reproducibility Data," an e-poster presentation to the June 2021 Symposium of the International Society for Therapeutic Ultrasound, and "Development of *in vitro* US Neuromodulation System with Concurrent Measurement of Evoked Local Field Potentials," an invited talk to the 2nd Symposium on Focused Ultrasound Neuromodulation in September 2021. Figures 7-9, 12, 18-19, and 23 are re-used from one or both of these presentations.

Contents

List of Figures

List of Abbreviations

1D,2D,3D ... one-dimensional, two-dimensional, three-dimensional
ACSF ... Artificial cerebrospinal fluid
BBB ... Blood-brain barrier
CAD ... Computer-aided design
CW ... Continuous-Wave [ultrasound]
dB ... decibel
DC ... Duty cycle
FEM ... Finite-element modeling
fEPSP ... Field excitatory post-synaptic potential
FUS ... Focused ultrasound
FWHM ... Full-width at half-maximum
HIFU ... High-intensity focused ultrasound
I_{SPTA} ... Intensity, Spatial-Peak Temporal-Average
I_{SPPA} ... Intensity, Spatial-Peak Pulse-Average
KCl ... Potassium chloride
LIFU ... Low-intensity focused ultrasound
LFP ... Local field potential
M ... Molar
MI ... Mechanical Index
MR ... Magnetic resonance [imaging]
MRgFUS ... Magnetic resonance-guided focused ultrasound
MRgHIFU ... Magnetic resonance-guided high-intensity focused ultrasound
MRI ... Magnetic resonance imaging
MEA ... Microelectrode array
mEFP ... Mean extracellular field potential
MUA ... Multi-unit spiking activity
NF ... Natural focus
NFHD ... NeuroFUS Hardware Design
NI-VISA ... National Instruments Virtual Instrument Software Architecture
PRF ... Pulse repetition frequency
PW ... Pulsed-Wave [ultrasound]
PZT ... Lead zirconate titanate
RF ... Radio-frequency
RMS ... Root-mean-square
TI ... Thermal Index
UV ... Ultraviolet [radiation]
VNA ... Vector network analyzer
V_{pp} ... Volts peak-to-peak

List of Symbols

Symbol	Meaning	SI Unit
α	Ultrasound attenuation constant	$dB \cdot cm^{-1} \cdot MHz^{-1}$
ρ	Density	kg/m^3
c	Speed of sound	m/s
d	Diameter	m
R	Reflection coefficient	*Unitless*
T	Transmission coefficient	*Unitless*
t	Time	s
MI	Mechanical Index	*Unitless*
f_0	Fundamental frequency	s^{-1}
F_{rad}	Radiation force	$N/m^3 = kg \cdot s^{-2} \cdot m^{-2}$
i	Imaginary constant	
I	Sound intensity	W/m^2
λ	Wavelength	m
p	Sound pressure	Pa
$\hat{p}$	Complex pressure	Pa
r	Radius	m
θ	Angle	rad
v	Particle velocity	m/s
$\hat{v}$	Complex velocity	m/s
ω	Angular frequency	rad/s
Z	Specific acoustic impedance	$Pa \cdot s \cdot m^{-3}$

1. Introduction

1.1: Focused Ultrasound

Generation of ultrasound. Ultrasound refers to oscillating mechanical pressure perturbations at a frequency above the human hearing range (greater than 20 kHz). Ultrasound is typically generated with a piezoelectric device or array of devices; piezoelectricity refers to the conversion between electrical and mechanical energy in certain crystalline materials. By applying an oscillating high-frequency electric field to the poles of a piezoelectric crystal, the crystal will experience a high-frequency compression and rarefaction that is transmitted to the surrounding medium (such as air, water, or tissue). This interaction is formally known as the inverse piezoelectric effect.

Plane wave acoustics. The characteristic impedance of a medium is a quantity measuring its resistance to energy flow; in a fluid medium, this is a resistance against the flow of acoustic energy. It is defined for a plane wave according to Equation (1.1) below, where specific impedance Z is a function of density ρ_0 and speed of sound *c* [1].

$$Z = \rho_0 c \tag{1.1}$$

When an acoustic wave encounters the boundary between two media with different impedances, some portion of the energy is reflected back and some amount may be transmitted. The dynamics of reflection are determined by the impedances of the media and also the angle of incidence, as shown in Equations (1.2), (1.3), and (1.4). In these equations, the plane wave originating in medium 1 encounters an interface with medium 2; the symbols θ, c, and Z refer to angle with respect to the normal, speed of sound, and impedance respectively; and the subscripts *i*, *t*, and *r* refer to incident, transmitted, and reflected respectively. The quantity R is known as the reflection coefficient and T is known as the transmission coefficient.

$$\sin\theta_t = \frac{c_2}{c_1}\sin\theta_i \tag{1.2}$$

$$\mathrm{R} = \frac{Z_2\cos\theta_i - Z_1\cos\theta_t}{Z_2\cos\theta_i + Z_1\cos\theta_t} \tag{1.3}$$

$$\mathrm{T} = \frac{2Z_2\cos\theta_i}{Z_2\cos\theta_i + Z_1\cos\theta_t} \tag{1.4}$$

When $c_2 > c_1$, there is a special case for some θ_i known as "total internal reflection" in which θ_t is imaginary, following from Equation (1.2); in this case, T will be exactly 0. This condition can be expressed as: total internal reflection will occur for $\theta_i > \sin^{-1}(c_1/c_2)$ [1]. For the case of waves propagating in water encountering a boundary with air, this limiting condition does not arise ($c_1 > c_2$);

however, for waves traveling through air and encountering a boundary with water, any waves oriented more than 14 degrees from the normal will be totally reflected.

Note that for the case of air and water, the difference in acoustic impedance ($Z_{\text{water}} \gg Z_{\text{air}}$) leads to $\mathrm{T} \approx 0$ and $\mathrm{R} \approx 1$ regardless of incident angle. This property is the basis of the device design described in Chapter 2, which aims to fix an air pocket of precise shape, enclosed in a thin plastic shell, in front of a flat piston-type transducer to focus the ultrasound wavefronts via reflection.

Computing the acoustic field. A baseline formulation of the governing physical equations can be obtained using differential equations corresponding to conservation of mass (also known as continuity) and conservation of momentum (also known as the equation of motion). In these equations density is denoted by ρ, velocity is denoted by v, pressure is denoted by p, and the operator D/Dt is the substantial time derivative (also known as the material derivative, representing the change in a property relative to fluid motion) [2].

Continuity, or conservation of mass, is described by Equation (1.5).

$$\frac{\partial \rho}{\partial t} + \nabla \cdot (\rho v) = 0 \tag{1.5}$$

Conservation of momentum, also known as the equation of motion (neglecting viscous forces) is described by Equation (1.6). g denotes the gravity force.

$$\rho \frac{Dv}{Dt} + \Delta p - \rho g = 0 \tag{1.6}$$

Equation (1.7) is a form of the resultant acoustic wave equation in Cartesian coordinates.

$$\frac{\partial^2 \rho}{\partial x^2} + \frac{\partial^2 \rho}{\partial y^2} + \frac{\partial^2 \rho}{\partial z^2} = \frac{1}{c^2}\frac{\partial^2 \rho}{\partial t^2} \tag{1.7}$$

One solution for Equation (1.7) is Rayleigh's integral (sometimes referred to as the Rayleigh-Sommerfeld diffraction integral), which models a vibrating surface surrounded on its plane by a solid baffle and which gives an equation for the time-varying pressure at any point beyond the baffle. It may be expressed in the form of Equation (1.8):

$$p(u,t) = \frac{\rho}{2\pi} \iint \frac{\dot{v}\left(x_s, y_s, t - \frac{R}{c}\right)}{R} dx_s dy_s \tag{1.8}$$

In Equation (1.8), $\dot{v}(x, y, t)$ is the normal velocity of the vibrating rigid surface, and R is the Euclidean distance from each integrating element to the query point u. x_s and y_s are the points making up the vibrating surface. Figure 1 illustrates these points and vectors relative to a vibrating disc.

Equation (1.9) shows the constant-frequency form of the Rayleigh integral, which is derived from the Helmholtz equation.

$$\hat{p}(u) = \frac{-i\omega\rho}{2\pi} \iint \frac{\hat{v}(x_s, y_s)}{R} e^{ikR} dx_s\, dy_s \tag{1.9}$$

In Equation (1.9), $\hat{p}$ denotes complex amplitude of acoustic pressure, $\hat{v}$ denotes complex velocity (normal) of the surface, u is the vector from the origin to the query point, and x_s and y_s are the points on the (circular) vibrating surface. ω represents frequency in radians per second and k is wave number ω/c.

Discretized, this formula may be interpreted as a summation of energy contributions from small vibrating elements making up the surface. This interpretation aligns with principles of scalar diffraction theory – specifically, the treatment of the radiating element as a collection of spherically-radiating point sources, and the resultant field being considered a superposition of their contributions [1]. A discretization of Equation (1.9) in cylindrical coordinates for a flat piston source can be written as in Equation (1.10).

$$\hat{p}(u) = \frac{-i\omega\rho v}{2\pi} \sum_{r=0}^{tx\ radius} \sum_{\theta=0}^{2\pi} \frac{A(r,\theta) e^{ikR}}{R} \tag{1.10}$$

In this formulation, A corresponds to the area of each radiating section, which depends on the discretization interval of r and θ.

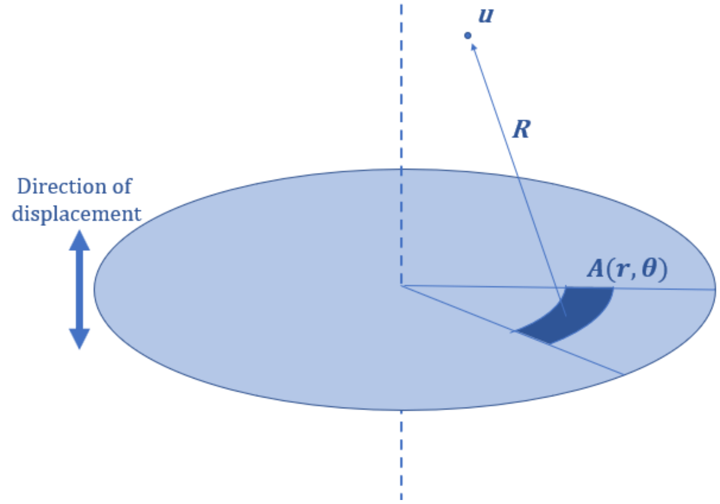

Figure 1: Discretization of a radiating disc in annular sections, corresponding to the syntax in Equation (1.10). R is the distance from the section to u.

Because the 3D solution is known to be rotationally symmetric, we can compute sample points only from one 2D plane (for example, θ=0). In the case of a flat piston-type transducer, this strategy has low computational complexity; the computation load increases greatly if we attempt to incorporate specular reflections, as in some of the simulations described in Chapter 2. When I apply the rule-of-thumb from finite-element and finite-difference schemes of 10 spatial points per acoustic wavelength [3], the free-field diffraction pattern for the transducer alone is solved by MATLAB in less than 2 seconds; however, introducing 10 reflecting elements rotated around the acoustic axis increases the computation time beyond 35 minutes. This time per evaluation is intractable for the purposes of rapid repeated computation within the optimization scheme I employ in Chapter 2. Furthermore, this strategy did not demonstrate accuracy on par with other evaluation techniques.

One prospective simplification of this system involves taking advantage of the rotational symmetry of the model system, and simulating only one slice of the transducer in the R-Z plane; however, note well that this symmetry only applies to determining the resultant pressure for the 1-D line through the isocenter – symmetry is violated for all other points. These two strategies – the 3D simulation that gives the symmetric 2D field, and the 2D model that gives the 1D field on the central axis – were employed in early phases of the design procedure detailed in Chapter 2.

Effects of ultrasound. Several physical effects can arise from the passage of ultrasound through a medium:

<u>(1) Establishment of an oscillating pressure field.</u> The medium through which the waves travel experiences a time-varying compression and rarefaction of its constituent particles. In liquid media, regions of high negative pressure (extreme rarefaction) may elicit *cavitation*, the formation of vapour bubbles. In living organisms, cavitation is typically considered a harmful bioeffect. Mechanical Index (MI) is a safety measure of ultrasound dosage that quantifies the exposure to cavitation-related bioeffects, and is calculated according to Equation (1.11). f_0 is the frequency of the carrier wave.

$$\mathrm{MI} = \frac{\text{Peak rarefactional pressure}}{\sqrt{f_0}} \tag{1.11}$$

The United States Food and Drug Administration-recommended safe MI for imaging ultrasound is 1.9 and below for most applications and 0.23 and below for ophthalmic applications [4]. The International Electrotechnical Commission 60601 standard provides a more stringent safety level for MI in diagnostic imaging applications, recommending MI below 0.3 to 0.7 [5].

Other quantitative measures of this oscillating pressure field include sound pressure (in Pascals) and sound intensity (in Watts per square meter). Pressure is a field quantity that is not directional, whereas sound intensity incorporates particle velocity, and therefore is directional. The fundamental relationship between the two quantities is shown in Equation (1.12).

$$\vec{\mathrm{I}} = p\vec{v} \tag{1.12}$$

p is the scalar measure of pressure, $\vec{\mathrm{I}}$ and $\vec{v}$ are vector quantities, and $\vec{\mathrm{I}}$ is defined as the intensity in a specified 2D plane for which $\vec{v}$ is the normal. For the plane perpendicular to the direction of ultrasound propagation in the plane wave case, magnitude of intensity is related to peak pressure by Equation (1.13). ρ represents density and c represents the speed of sound in the medium.

$$\left|\vec{\mathrm{I}}\right| = \frac{\left|p_{\mathrm{peak}}\right|^2}{2\rho c} \tag{1.13}$$

For ultrasound emissions that are modulated by a rectangular pulse train – occasionally referred to as pulsed-wave (PW) ultrasound, in contrast to continuous-wave (CW) ultrasound – there is a distinction between the intensity measure over a unit of time, which is the spatial-peak temporal-averaged intensity (I_{SPTA}), and the intensity measure normalized to only the “on” phases, which is the spatial-peak pulse-averaged intensity (I_{SPPA}). The United States Food and Drug Administration also recommends safe maximum levels for these two measures in imaging ultrasound, varying based on imaging target [4].

(2) Wave attenuation. Absorption of energy carried by the travelling wave leads to two major effects in the medium: thermal energy deposition and acoustic radiation force. Ultrasound-induced heating of biological tissue is sometimes the primary desired effect of the FUS treatment; ablative and hyperthermia applications of ultrasound are further discussed in the sub-section on high-intensity focused ultrasound (HIFU). In terms of safety guidelines, ultrasound-induced heating is quantified by Thermal Index (TI), which is defined according to the worst-case peak temperature rise in degrees Celsius; temperature rise in perfused biological tissue is often estimated according to the bio-heat transfer equation, which is reproduced in Equation (1.14); in (1.14), T is temperature, k_{cond} is the thermal conductivity coefficient, and the Q terms refer to heat flux from blood perfusion, metabolic heat generation, and the heat contributed by the procedure respectively [6]. Safety recommendations for temperature vary based on application and based on duration of exposure to heating [7] .

$$\rho c \frac{\partial T}{\partial t} = \nabla(k_{\mathrm{cond}} \nabla T) + Q_{\mathrm{perfusion}} + Q_{\mathrm{metabolic}} + Q_{\mathrm{in}} \tag{1.14}$$

Energy absorption also generates acoustic radiation force. In a homogeneous medium, acoustic radiation force manifests as a net pushing motion in the direction of ultrasound propagation. It is proportional to intensity I and to a frequency-dependent attenuation coefficient α, and inversely proportional to the speed of sound c, as shown in Equation (1.15).

$$\mathrm{F}_{\mathrm{rad}} \propto \frac{I\alpha}{c} \tag{1.15}$$

Note that radiation force $\mathrm{F}_{\mathrm{rad}}$ is a body force exerted equally throughout a volume, and therefore defined in Newtons per cubic meter ($kg \cdot s^{-2} \cdot m^{-2}$) [8].

Transducer construction principles. In the physical construction of an ultrasound device, the material conditions at the back and at the front of the piezoelectric crystal are both relevant to its performance. The choice of backing material affects the damping performance of the device, which is directly related to the bandwidth of the device. Driving of transducers for ultrasonic imaging uses short pulses which are damped by a backing material, corresponding to a wide bandwidth that is more suitable for imaging; transducers for ultrasonic therapy are more commonly air-backed, corresponding to a narrower bandwidth and a larger amplitude total displacement [9], [10].

The surface of the transducer in contact with the transmission medium can be fitted with a matching layer to improve conduction of the induced vibration. To maximize transmission for a single frequency, the optimal design involves a matching layer with thickness equal to exactly $\lambda/4$ and with characteristic impedance equal to the geometric mean of the two impedances being interfaced. It is also possible to install multiple matching layers for reasons related to bandwidth [11].

Focusing ultrasound. Strategies for controlling and focusing the resultant pressure field, and thus achieving focused ultrasound (FUS), can be generally grouped into three categories.

(1) Shaped crystal. Spherically-focused transducers, which have one surface molded to the shape of a concave spherical section, have historically been the most prevalent method of FUS production. The resultant pressure field is most intense in a cigar-shaped region some distance away from the curved surface, demonstrated schematically in Figure 2.

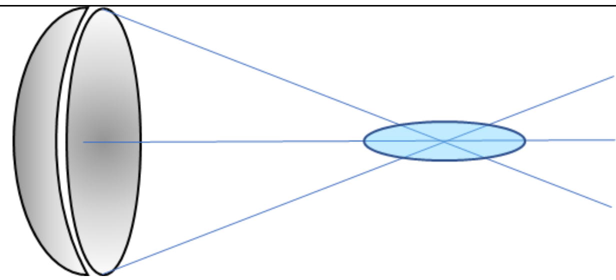

Figure 2: Schematic diagram demonstrating ultrasound focusing via a shaped transducer.

Note that a transducer with a flat surface also produces a natural focus (NF) at the transition between the near-field and far-field propagation zones. The position of the NF is determined for a flat cylindrical transducer by its operating frequency and diameter: a common estimate for the length of the near-field zone is $D = diameter^2/4\lambda$.

(2) Phased array. By arranging many smaller transducer elements and controlling them independently, one may attain improved control of the resultant ultrasound wave patterns [12], [13]. This technique of independent control is frequently referred to as electronic steering of ultrasound. The assembly of transducers is known as a phased array, in reference to the application of phase delays to individual driving signals (see Figure 3A). The ability to apply steering has additional relevance to transcranial treatments: the phase-based steering can be used to partially cancel distortion caused by skull bone, greatly improving the ability to non-invasively focus ultrasound within living brains [14], [15] (see Figure 3B).

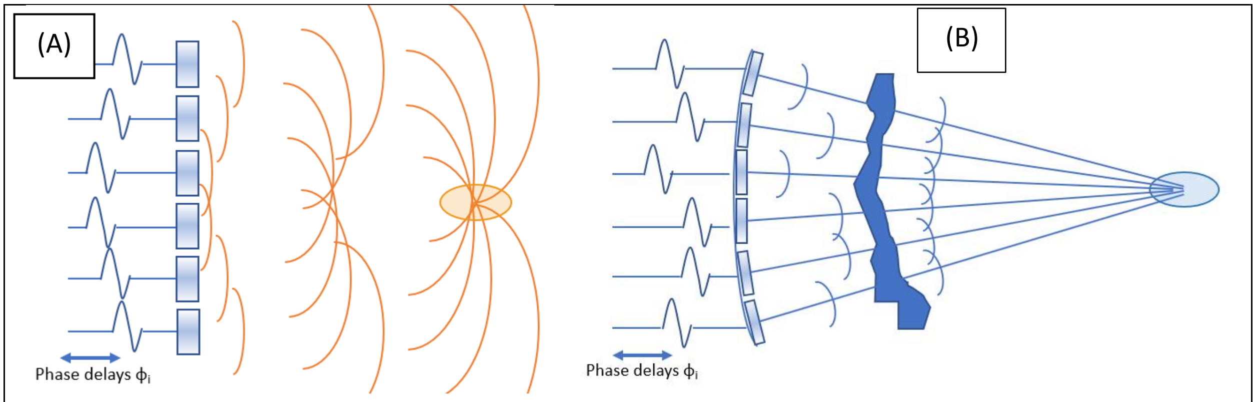

Figure 3: Phased arrays. (A): schematic diagram demonstrating a linear phased array using various delays along the line to cause wavefronts to converge. (B): schematic diagram demonstrating a phased array cancelling skull aberration.

(3) External collimation. An improved ultrasound focus can be obtained from any of the transducer settings mentioned above – single-element flat, single-element curved, or multi-element array – via application of a lens or coupling to change the trajectory of the acoustic waves. There is close overlap between the principles of phased array design and acoustic lens design: an elliptic or spherical lens can produce a narrow focus from a planar source [16], [17]; and a lens with many partitions can be computed to cancel phase aberrations, such as in the transcranial case [18]. These types of refracting focusing devices are often cone-shaped, and may be composed of a gel (e.g. the agarose gel waveguide-style collimator used by Suarez-Castellanos et al. in [19]) or a solid segment (e.g. the Rexolite cone used by Lin et al. in [20]). The technique explored in Chapter 2 and employed in Chapter 3 falls under this category of external collimation.

Overview of FUS in medicine. The earliest experiments into effects of ultrasound on biological tissue demonstrated its potential to rapidly kill small animals [21], [22]. Harvey [23] demonstrated a non-thermal effect of ultrasound exposure in 1929. In 1942, Lynn et al. [24] used FUS to produce localized heating in beef liver and animal brain samples, and proposed improvements to their system “to produce local changes in tissues … or in the brain … with a minimum of complicating injuries to superficial tissues.” The eventual therapeutic practice of producing lesions in tissue is referred to as HIFU ablation; currently, HIFU ablation is approved for the treatment of uterine fibroids and as an adjuvant therapy for several cancers. A relevant component of HIFU treatments is live temperature monitoring, which is often acquired by simultaneous MRI thermometry, thus the treatment is designated MR-guided focused ultrasound (MRgFUS or MRgHIFU) [25]. In non-brain tissue, lesioning is a result of temperature-rise-induced coagulative necrosis. Thermal dosage of cancer treatments was found to have an exponential relationship with time: a 60-minute treatment at 43 °C is considered equivalent to a 30-minute treatment at 44 °C and to a 15-minute treatment at 45 °C [26]. Non-thermal procedures involving HIFU include shockwave lithotripsy for destruction of kidney stones [27] and boiling histotripsy for nonthermal ablation [28].

Non-lesioning HIFU can still produce therapeutically relevant temperature increases in the family of procedures known as ultrasound hyperthermia [29], [30]. Hyperthermia can enable targeted drug delivery, for example drugs enclosed in thermosensitive liposomes; it is also investigated for its ability to promote localized immune response and blood flow [31], [32].

1.2: FUS in the brain

Overview of FUS in the brain. Some of the earliest surgical explorations of FUS occurred in the context of brain surgery, [33] but were hampered by a lack of adequate imaging technologies and the need for skull resection or craniotomy. Work by Fry and Goss in 1977-1981 advanced the possibility of trans-skull procedures, and the development of phased arrays (described in the above section "Focusing ultrasound") further realized noninvasive ultrasound procedures in the brain. Pre-clinical tests for modern HIFU brain surgery were conducted in 2006 with the ExAblate 2000 (InSightec Inc., Haifa, Israel) [34]. Ablative HIFU is currently used in the brain as an approved treatment for essential tremor [35], [36].

One therapeutic procedure that is unique to the brain is blood-brain barrier (BBB) opening with low-intensity focused ultrasound (LIFU), which can enable the delivery of therapeutic agents that are normally difficult to deposit in the brain. Ultrasound-induced BBB opening was first documented in 1956 [37] and first successfully integrated into an MR-guided system in 2001 [38]. FUS-induced BBB opening has demonstrated therapeutic benefit even without drug delivery [39].

Neuromodulation. The practice of using external stimuli – including electrical, chemical, magnetic, and other types of agents – to control or modify nervous system function has been used to develop diverse therapeutic applications and to study brain activity. The terms "neuromodulation" and "neurostimulation" have been applied to describe this concept, with terminology varying based on journal, specialty, era, and other factors. Following the definition provided by Krames et al. in 2009 [40], in this document "neuromodulation" will be used to describe the family of treatments that lead to reversible and non-destructive modification of nervous system function. Neuromodulatory treatments are employed in the normal treatment course for chronic neuropathic pain [41]–[43]; neuromodulation is also explored as an adjuvant therapy for conditions including epilepsy [44], depression [45], [46], obsessive-compulsive disorder [47], and certain symptoms of Parkinson's disease [48], [49].

The possibility of ultrasound-induced neuromodulation was detected as early as 1958 [50], when the Illinois research group led by the Fry brothers documented a reversible effect of ultrasound on nervous tissue at lower intensities. Both the Fry group and other contemporary researchers documented permanent damage at high ultrasound intensities, but reversible effects at lower intensities, such as the 1960 experiments by Ballantine et al. in cats [51]. Studies between 1977 and 1984 by Gavrilov et al. [52]–[54] tested and characterized ultrasound stimulation of the peripheral nervous system at moderate intensities, including assessments of safety on humans. The use of ultrasound to produce neuromodulatory effects is appealing because LIFU combines fine spatial resolution and non-invasiveness. The physics associated with comparable non-invasive brain treatments (including transcranial magnetic stimulation and transcranial direct-current stimulation) limit their precision to foci on the order of centimeters, while ultrasound foci may be produced on the order of millimeters at usable frequencies [55]. Relative to these other stimulation techniques, focused ultrasound neuromodulation has minor drawbacks: it requires at least partially shaving the recipient's head, which transcranial magnetic stimulation (TMS) does not mandate; and the treatment focality of FUS is limited by the frequency used (discussed further in Chapter 2.2 § "Considerations for Transducer Selection") and by uncertainty in the mechanism of action causing uncertainty in the treatment volume (discussed briefly in Chapter 2.3 § "Design of the Hardware Optimization Scheme" and immediately below in "Proposed mechanisms of ultrasound neuromodulation").

Technique	Non-invasive?	High Spatial Resolution?
Deep-brain stimulation	×	✓
TMS	✓	×
TDCS/TACS	✓	×
Focused ultrasound	✓	✓

Table 1: Characteristics of neuromodulatory treatment families.

Proposed mechanisms of ultrasound neuromodulation. The dominant biophysical mechanism(s) underlying ultrasound neuromodulation are currently not known. Many hypotheses and theories have been developed to explain the effects of LIFU in different model organisms, but experimental evidence does not conclusively point towards any one framework. The effects of ultrasound on nervous tissue are known to be highly dependent on timing and intensity parameters; furthermore, the variety of effects seen in different experimental settings are likely explained multi-modally; these two complicating factors account for much of the difficulty in conclusively establishing dominant mechanisms.

One family of hypotheses concerns specific cellular targets found endogenously in the nervous system. Various ion channels are known to have mechanosensitive properties, and studies have demonstrated that LIFU can actuate Piezo1, Na_v1.5 and the family of 2-pore-subdomain K^+ channels, and astrocytic TRPA1 [56]–[59]. Channel blockers such as tetrodotoxin and cadmium ions were applied in brain slices and in animals to largely cancel the effect of ultrasound, further implicating direct actuation of ion channels [60], [61]. The physical mechanism associated with this biophysical explanation is the acoustic radiation force [62].

Several hypotheses have arisen that are primarily simulation-based or physics-based. The intramembrane cavitation model suggests that the layers of neurons' bilayer membranes are pulled apart by ultrasonic pressure [63]–[65]. Similarly, Prieto et al. suggest in 2013 that the membrane capacitance can vary with ultrasonic radiation force [66], and several researchers have observed an ultrasound-induced change in membrane conductance [20], [67], [68]. Another modeling-based hypothesis treats neural action potential propagation as a mechanical and thermal phenomenon, and thus accounts for the ability of LIFU to modulate and induce neural activity [69], [70].

Radiation force as the physical mechanism of ultrasound neuromodulation has a strong associated body of experimental evidence. Menz et al. [71] used optical imaging to detect a 4-µm displacement induced by radiation force in salamander retina. The physical phenomenon of radiation force is incomplete by itself: it does not explain the influence of pulsed FUS timing parameters – for example, Yu et al. [72] varied LIFU pulse repetition frequency while maintaining I_{SPTA} constant in one study and while maintaining I_{SPPA} constant in another study, and in both studies there was a positive trend in neuronal spiking rates with increasing pulse repetition frequency. This influence of timing parameters on responses, as well as the widespread use of pulsed-wave over continuous-wave FUS in experiments, suggests that the presence of a net pushing force may not be as important as the time-characteristics of this oscillating force.

Electrophysiological recordings. To detect and quantify brain activity, electrical signals in nervous tissue may be recorded in several different ways. Single-unit recordings capture activity from a single neuron, most typically by establishing an intracellular interface with a microscopic conductor; one of the most well-known categories of intracellular single-unit recording is patch-clamp recording, and there are further sub-categories based on how the intracellular interface is set up. In the context of studying focused ultrasound, it is challenging to apply patch-clamp measurement techniques: the seal between the electrode and the cell is easily disturbed by ultrasonic stimulation at typical frequencies and intensities [56]. Tyler et al. [60] successfully did whole-cell patch clamp of a CA1 pyramidal hippocampal neuron during FUS, and Prieto et al. [56] applied ultrasound stimulation to cultured cells expressing certain neuronal ion channels, but this type of study constitutes a minority in the field due to the aforementioned challenges. More typically, a microelectrode array (MEA) comprising many conducting shanks is applied, usually with cultured tissue (which can be grown on the MEA); each electrode on an MEA is considered a single-unit extracellular recording.

Extracellular electrophysiological recordings involve the insertion of a conductor into the extracellular space. The output signal is a mean extracellular field potential (mEFP). The size of the electrode tip dictates the number of cells contacted and the diffuseness of the signal measured. The mEFP signal may be separated out into the high-frequency components (greater than 300-500 Hz) which are referred to as multi-unit spiking activity (MUA), and lower-frequency components (less than 300 Hz) which are referred to as local field potentials (LFPs) [73], [74]. MUA is considered very spatially localized: it contains the extracellular action potentials of neurons within a few hundred microns of the electrode tip. LFPs instead reflect “cooperative activity” [73] and “slower oscillations” [74] in the neural tissue, and it is known today that most LFP activity originates from remote current sources rather than ones local to the electrode [75]. Several FUS studies have investigated LFPs, both in *de novo* contexts (i.e., experiments in which ultrasound induces coordinated neural activity) and evoked contexts (i.e., experiments in which ultrasound modifies coordinated neural activity). Several studies [61], [76], [77] have demonstrated the ability of FUS to induce LFPs *de novo*. At least two studies [78], [79] have also demonstrated the ability of FUS to modulate electrically-evoked LFPs. Other electrical field indices of neural activity are frequently studied, including visual evoked potentials [50] and somatosensory evoked potentials [80], but these are different models of neural signal transmission and cannot be directly compared with LFPs.

In Chapter 3, I detail our experiments in which we use LIFU to modulate electrically-evoked LFPs.

1.3: Summary of Chapters

Chapter 2 of this thesis describes the technical development of a transducer, collimator, and basin system custom-designed for experiments into LIFU neuromodulation in brain slices. Chapter 3 presents the results of brain slice experiments intended to characterize the modulation effects we elicited, and also intended to validate the performance of the custom system. Chapter 4 summarizes and further contextualizes these developments and results. The appendices to this document (Appendix A "User Manual" and Appendix B "Hardware Developer Manual") are necessary resources for the continued maintenance and application of this system to neuroscientific experiments involving ultrasound at the University of Calgary.

1.4: Statement of Contribution

Chapter 2 ("Development of a Computer-Optimized Experiment Platform for Ultrasound Neuromodulation Studies") builds on a simulation and optimization procedure originally designed by Alan Coreas from May 2018 to August 2018; over the course of my thesis work from September 2018 onwards, I replaced almost every part of this initial design, including the optimization components, the cost function evaluation, and the elements to simulate the system. The construction and validation work described in this chapter made significant use of equipment, time, and laboratory resources generously contributed by Dr. Laura Curiel. Catherine Swytink-Binnema and Dr. Zelma Kiss contributed feedback on the physical and functional aspects of the device described in this chapter. Catherine Swytink-Binnema also contributed engineering drawings and design concepts that were incorporated into the component referred to as the "mesh basin."

Chapter 3 ("Replicability Study: Ultrasound-Induced Modulation of *in vitro* Evoked Local Field Potentials") describes neuroscientific experiments primarily designed and conducted by Catherine Swytink-Binnema and overseen by Dr. Zelma Kiss. I contributed to the design of the control conditions.

2. Development of a Computer-Optimized Experiment Platform for Ultrasound Neuromodulation Studies

Jak Loree-Spacek,[a] Catherine Swytink-Binnema,[a] Laura Curiel,[b] Zelma Kiss,[c] Alan Coreas,[b] Samuel Pichardo[d]

[a] Biomedical Engineering Graduate Program, University of Calgary, Calgary, Canada
[b] Dept of Electrical and Computer Engineering, Schulich School of Engineering, Calgary, Canada
[c] Dept of Clinical Neurosciences, Cumming School of Medicine, Calgary, Canada
[d] Depts of Radiology and Clinical Neurosciences, Cumming School of Medicine, Calgary, Canada

2.1: Abstract

Our lab group conceived of a method for focusing ultrasound via an external reflecting apparatus. This technique was appealing on the grounds of its novelty, customizability, and cost-effectiveness. Our group envisaged this novel focusing technique being applied to experiments involving simultaneous ultrasound stimulation, electrophysiological recording, and microscope observation of animal brain slices. Towards this goal, I applied a combination of optimization and simulation techniques to generate a series of "equally optimal" solution geometries. I chose one feasible design for production and validation based on the needs of the neuroscientific experiments to follow, and I validated the chosen geometry using 3D hydrophone measurements to verify the shape of the pressure field. I characterized the absolute intensity of this pressure field with two independent methods, and performed all other characterization tests necessary to deliver predictable ultrasound doses across the operating range.

In this research chapter, I describe the development processes for the computer simulations, the hardware components, and the implementation of the custom system; I also report the completion of validation and compatibility tests to ensure the system functions suitably under experimental conditions.

2.2: Introduction

Objectives. Our lab group at the University of Calgary, led by Dr. Samuel Pichardo, sought to work together with Dr. Zelma Kiss from the Hotchkiss Brain Institute on conducting LIFU neuromodulation experiments. The Kiss Lab would contribute their brain recording experience and equipment, and our lab committed to the development of a custom ultrasound device to enable suites of upcoming experiments. The high-level goals of such experiments were known in advance: our lab groups sought greater understanding of mechanisms and effective parameters of LIFU neuromodulation by using a specific model organism (acute rat brain slices).

In parallel, our group had devised a novel technique for obtaining custom ultrasound foci: a reflective collimator consisting of a shaped air pocket. This technique supposedly imparted the advantages of acoustic lens strategies (low cost, rapid development time, and high customizability), but with one additional comparative advantage that practically no ultrasonic energy is lost via attenuation or diffraction out the sides. We wanted to explore the potential of this technique and simultaneously develop a usable system for LIFU experiments in rat brain slices.

Design goals. The requirements of the eventual brain slice experiments imposed certain design targets and constraints.

<u>Performance goals:</u> The slices of rat hippocampus and cortex that we obtain from standard slicing protocols are at most 1.5 cm by 1 cm (sliced to ~350 µm thick), and the brain structures we are targeting are on the order of a few cubic millimetres. Thus, for the sake of experimental design, a smaller focal region is better; if possible, in our experiments we would prefer to insonate only a 1-2 mm^2 cross-sectional region of the slice (i.e. highly focused in the axial plane, less necessary to be focused laterally). To achieve these performance goals, we devised a strategy to combine finite-element modeling (FEM) with mathematical optimization techniques to yield optimized hardware designs.

<u>Compatibility goals:</u> My other main goal in the design process was to ensure compatibility with the electrophysiology and microscopy experimental system. Figure 4 demonstrates the optical and space constraints encountered: a line-of-sight through the brain slice is necessary for consistently positioning the stimulating and recording electrodes. The micromanipulator-mounted electrodes point obliquely down into the slice from above, which also limits the possibility of positioning an ultrasound device in the same orientation. The artificial cerebrospinal fluid (ACSF) that sustains the brain slice must flow only a few mm above the top of the slice. The full system, including the ultrasound transducer, any necessary

focusing apparatus, and any other necessary structural apparatus to hold the brain slice and the ACSF must fit within the approx. 5.9 cm of total vertical room.

Figure 4: Schematic representation of the space constraints imposed by the target experiment setup. There must be a clear line of sight through the brain slice, thus the ultrasound device must not cross into the orange zone; the surface of the ACSF that sustains the slice must only flow a few mm over the top. Approaches similar to *in vivo* brain experiments – e.g., a gel-filled or polymer-filled channel pointed downwards at the sample – do not appear feasible here, so the entire device must stay confined to the fluid domain (below the blue dashed plane).

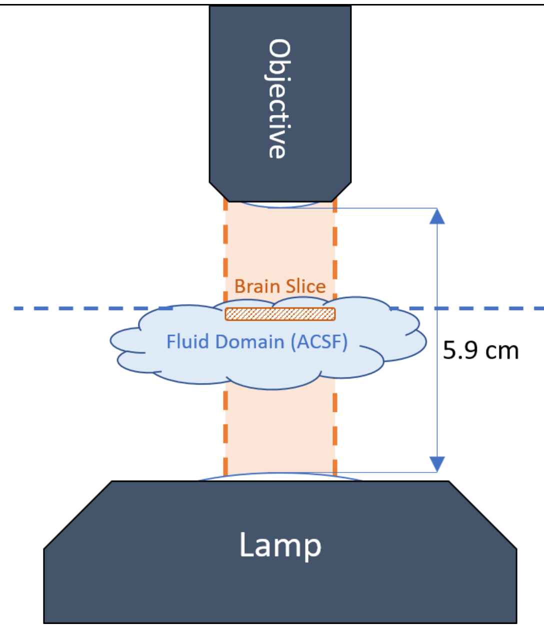

The electrophysiological recording system – and, to some extent, the rat brain slice itself – is sensitive to electrical signals on the order of mV and μV, and the transducer is excited by tens-to-hundreds of volts only a few centimetres away. Ensuring the ultrasound system does not introduce confounding electrical energy or patterns to the electrophysiology system is a major design goal. Ultimately, this electrical compatibility condition is fulfilled by a combination of design precautions (described in this chapter) and experimental design controls (described in Chapter 3).

Other goals: In the interest of rapid iterative development, ease of maintenance, and ability to translate components to different setups later, I aimed to make the ultrasound system as modular as possible. I also wanted to ensure the full system remained usable by non-engineering research staff; this goal constituted producing adequate documentation and also a front-end software console to streamline computations.

Considerations for transducer selection. The frequencies typically chosen by researchers investigating ultrasound stimulation of nervous tissue are between 100 kHz and 5 MHz, with a few studies working at a range closer to 50 MHz. From a physical perspective, a higher frequency offers higher spatial selectivity due to the shorter wavelength, but also leads to higher attenuation in most media. In applications requiring ultrasound to cross intact skull bone, attenuation by the bone is highly relevant [81], [82]; absorption of energy can lead to undesired heating of the skull. On the other hand, this frequency-attenuation relationship is also present in the brain tissue targeted for treatment: desired thermal and radiation force effects also change proportionally with frequency. This is relevant to frequency choice for neuromodulation because at least one hypothesis has implicated radiation force as a potential physical driver of neural responses. From a functional perspective, studies that perform parametric variation of frequency have shown improved motor neural responsiveness *in vivo* at lower frequencies tested [83]; this functional result was the primary factor informing our *a priori* choice of frequency for this development process. Finally, from a safety perspective, frequency appears in the definition of ultrasonic mechanical index, a quantity used to dictate safe intensity levels for imaging and therapy; in loose terms, the same peak pressure induces less cavitation at higher frequencies. This, too, has double-edged mechanistic implications: at least one hypothesis suggests a form of cavitation mediating certain bioeffects [63], [64], although this hypothesis is lacking experimental validation [62].

The chosen transducer diameter is relevant for a few reasons: first and foremost, that a particular experimental setup may impose a size restriction on the eventual device. As discussed above, the setup in which we conduct rat brain neuromodulation experiments does impose a stringent size restriction. The second concern involves the property of natural focusing; the natural focus (NF) is found at the transition between the near-field and far-field propagation zones. The position of the NF is determined for a flat cylindrical transducer by its operating frequency and diameter; as discussed in Chapter 1, for flat piston-type transducers, the relationship with frequency is linear, but the relationship with diameter is quadratic. Our *a priori* estimates regarding an appropriate frequency and diameter for transducers led to an NF that was extremely close to the transducer surface (approximately 3 mm). It was not clear how this property would interact with our external focusing device, so we considered only the space constraint and procured transducers with 10 mm diameter.

Optimization principles. The field of optimization (sometimes “mathematical programming”) [84] describes problems for which a minimum or maximum value solution is desired and for which an analytical approach may be infeasible. An optimization problem can be characterized by its input variable(s) and its desired output value(s). The input variables comprise the domain of the function under examination, and it is common for linear and non-linear constraints to be imposed upon them to limit the domain. The output of the optimization procedure is a guess or set of guesses at the position of the desired optimum. For linear and non-linear differentiable functions, iterative algorithms exist that converge to local optima, including the steepest-descent method [85] and the Levenberg-Marquardt algorithm [86]. Any problem space for which the obtained local minimum is not necessarily the global minimum of the whole space is termed a nonconvex optimization problem [87]. Approaches to global (nonconvex) optimization may be deterministic or stochastic: the former category includes algorithms such as the branch-and-bound algorithm, which search the entire problem space and converge in finite-time; the latter category includes the family known as multi-level single linkage algorithms, which semi-randomly search the problem space and finish in fixed-time [87]. A sub-category of stochastic global optimization is genetic algorithms, which are sometimes referred to as a heuristic optimization method because of the property of iterative improvement on candidate solutions [88]. Given that each evaluation is on the time-order of seconds for the scheme developed in this chapter, the speed at which a genetic algorithm arrives at a set of viable solutions is considered a relevant advantage. The importance of finding a globally-optimal solution versus an adequate locally-optimal solution is specific to the nature of the problem; in engineering applications, a locally-optimal solution may meet the requirements of a particular application, which may lessen the need for a global search.

When it is desired to optimize for several criteria simultaneously – problems referred to as multicriteria or multiobjective optimization problems – the task of finding suitable minima is further complicated, as it is somewhat improbable that two or more criteria will align well in the placement of their optima. The best attainable solutions in these cases are known as nondominated or Pareto-optimal solutions; this set of solutions, sometimes known as a Pareto front, is a set of points for which no other point exists in that set which improves on all outcome measures. A graphical representation of this concept for a two-objective problem is pictured in Figure 5. Such a set does not offer a conclusive optimum, and also does not inherently consider the relative importance of each objective.

Figure 5: An example of a Pareto front for a multi-criterion problem aiming to maximize two quantities. The red points A through H are considered Pareto-optimal; within the set of points, improvement in one criterion is accompanied by damage to the other criterion. Point N is outperformed by point E in both criteria, thus it is not part of the set.

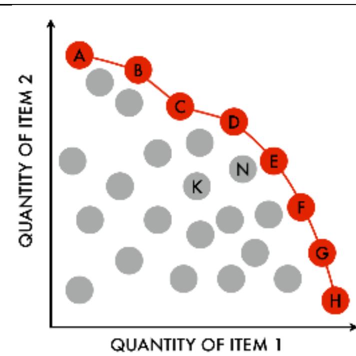

In light of preliminary tests suggesting the solution space to be highly erratic, I chose a multi-objective genetic algorithm for the hardware optimization scheme.

2.3: Methods

Design of the Hardware Optimization Scheme. Towards the optimized design of a reflective collimator, I built several models based on time-independent 2D and 3D Rayleigh integral methods between 2018-2019, and concurrently tested various optimization schemes and approaches. These models were parametrized in terms of a series of 100 contiguous lines representing the reflecting boundary in an axisymmetric manner, with each segment's angle treated as a separate parameter. To reduce the dimensionality of the problem space, I used a type of spline interpolation to generate 100-element "fine" geometries from 6-variable "coarse" geometries via MATLAB's `pchip` (Piecewise cubic Hermite interpolating polynomial) function. The reduction of dimensions in this manner is beneficial for any optimization problem, and it was hypothesized that the splined geometries would offer a set comparable to highly-parametrized geometries.

The chosen optimization scheme is MATLAB's `gamultiobj`, a function that implements genetic multi-objective global optimization. Modeling of the physical system is offloaded to COMSOL Multiphysics 5.4 (COMSOL Inc., MA, USA), a finite-element modeling software suite. The two programs communicate using the *LiveLink for MATLAB* interface. Upon each evaluation of the cost function on a particular iteration, the geometry is passed to COMSOL in the form of a 2D axisymmetric finite-element model. The model – pictured in Figure 6 – applies the parametrized geometry to generate a shaped air gap, fills the rest of the test domain with water, and applies appropriate radiation conditions at the boundaries. The domain is automatically meshed with a maximum element size of 1/6th the ultrasound wavelength for the aqueous domains (approx. 1.2 mm), and 1/10th the ultrasound wavelength in the air-filled domains (approx. 0.17 mm). The model is evaluated with a frequency-domain analysis, corresponding to the steady-state solution of the simulated system. Due to the relative computational simplicity of this system (2D axisymmetry and only linear elastic fluid domains under consideration), each evaluation took 5-8 seconds on desktop computer hardware. The MATLAB script then retrieves pressure values from the simulation environment by querying interpolation points from the finite-element grid.

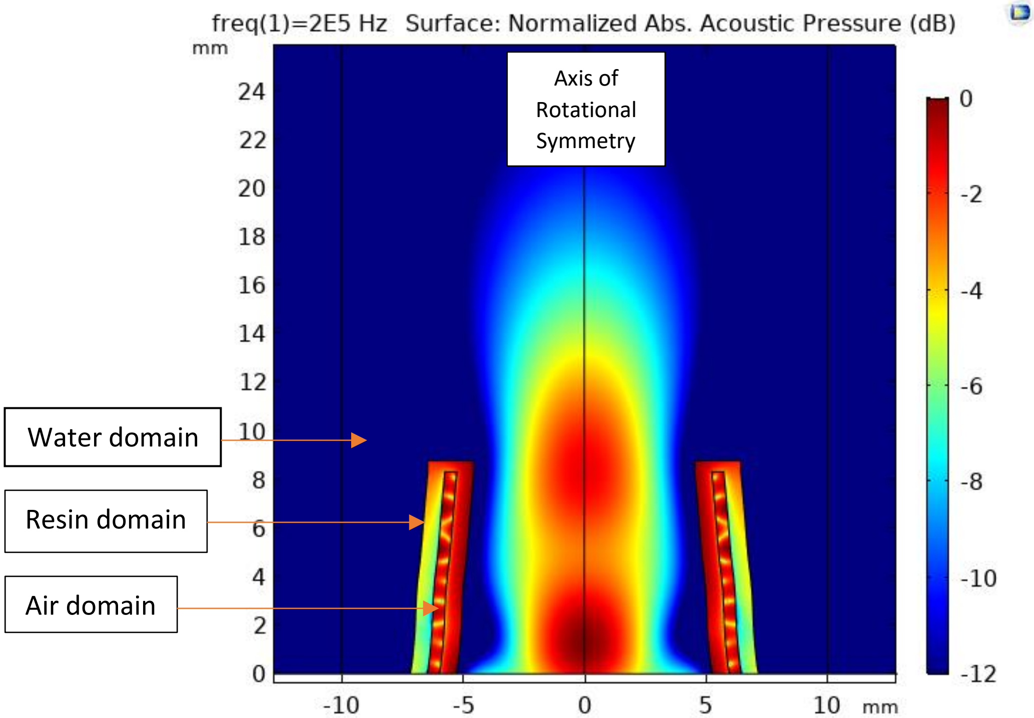

Figure 6: COMSOL 5.4 axi-symmetric model of air-pocket reflector. Transducer is modelled by a vibrating surface spanning -5 to 5 at Z=0. For rapid computation, all regions are treated as linear elastic fluid domains with appropriate density and speed-of-sound; relative pressure values in this graph are normalized per-domain.

The cost function evaluates both the length and width of the focal pressure region, aiming to maximize the former and minimize the latter. Following other literature on LIFU system development, it defines the focal region as the zone in which magnitude of pressure is greater than half of maximum (FWHM, "full-width at half maximum"). Some researchers [89], [90] have found that the 90%-intensity threshold (i.e., the 95% pressure threshold) is a better indicator of the spatial effects of neuromodulatory ultrasound, but FWHM of pressure is more standard, and relative physical measures will continue to be imprecise so long as the mechanisms of LIFU neuromodulation are uncertain. The MATLAB script requests a query grid of absolute acoustic pressure (COMSOL: `abs(acpr.p_t)`) covering the focal spot with uniform spacing of 0.25 mm in both axes. The query grid is normalized and MATLAB's built-in contouring algorithm is used to determine a 2D interpolated contour; the length of this interpolated contour is used directly as the length measure, and the width of the contour at halfway to the maximum extent was used for the width measure. The 2D contouring strategy was beneficial to the optimization because it smooths the optimization solution space better than methods that obtain length and width via counting. To disincentivize zero-width solutions, a reciprocal term was added to the width measure; the reciprocal term was scaled such that 0.5-mm-width solutions would be relatively unaffected, but less-than-0.1-mm width solutions would score significantly worse than 1.0-mm width solutions. Logic was also added to ensure that the script functioned consistently even if multiple contours were generated, such as in cases where the focal region comprised two or more distinct regions. Figure 7 demonstrates this contouring and the chosen definitions for length and width.

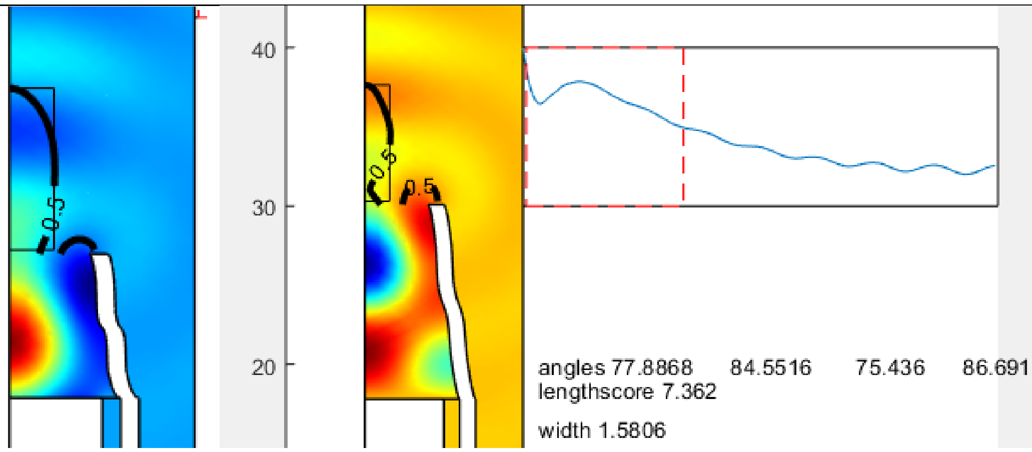

Figure 7: Two instances of scoring the extracted pressure field from two different reflector geometries. Measurement starts from the end of the focusing air gap; the rounded lines are the outputs of MATLAB's built-in 2D interpolating contour function, and the overlaid rectangles show the corresponding length and width measures. Inlaid plot on the right figure shows the pressure distribution in 1D in the axial direction at the central axis. Plot colouring is according to positive and negative pressure regions in the frequency domain solution.

Computer-aided design and fabrication. I designed three modular components to comprise the physical system: the collimator cone, a transducer backing to be affixed to the cone, and a custom basin into which the transducer assembly can be mounted. The air pocket shape chosen from the optimization output was translated into a computer-aided design (CAD) drawing in Fusion 360 (Autodesk Inc., San Rafael, CA, USA). To enable the 3D printing process, the drawing for the cone also features eight vent holes in the plastic enclosing the air pocket. The inner wall of the plastic enclosing the pocket is 0.40 mm thick, and the outer wall is 0.70 mm thick. Three holes accommodate three screws intended to connect the cone to the transducer backing.

The design for the transducer backing includes three cavities for pressure-fit threaded inserts, corresponding to the connecting screws. To improve the fit with the cone, there is a 0.5 mm-tall radial tongue-and-groove near the inner wall of the air pocket. The transducer backing also features an indentation to install a nitrile O-ring for a fluid-proof connection to the experiment basin.

The experiment basin was designed with a slot for a 1 mm glass slide to be glued into place, upon which the brain slice sits. A second section of 1 mm glass slide is glued into place on the bottom, making an optical window. It contains a shallow circular indentation corresponding to the O-ring on the transducer assembly and corresponding to the main fixed position of the transducer. In later revisions, I added a second O-ring indentation as a second position for the transducer. The second position (referred to as the “retraction position”) was intended so that the transducer could be pulled even further out of the line-of-sight during setup of the brain slice. It also contains a small tubular hole to hold the ACSF inlet pipe in place. We also designed and built an alternate experiment basin design in which the slice would be suspended on nylon mesh instead of glass; the usage of the mesh basin variant is described further in Chapter 3.

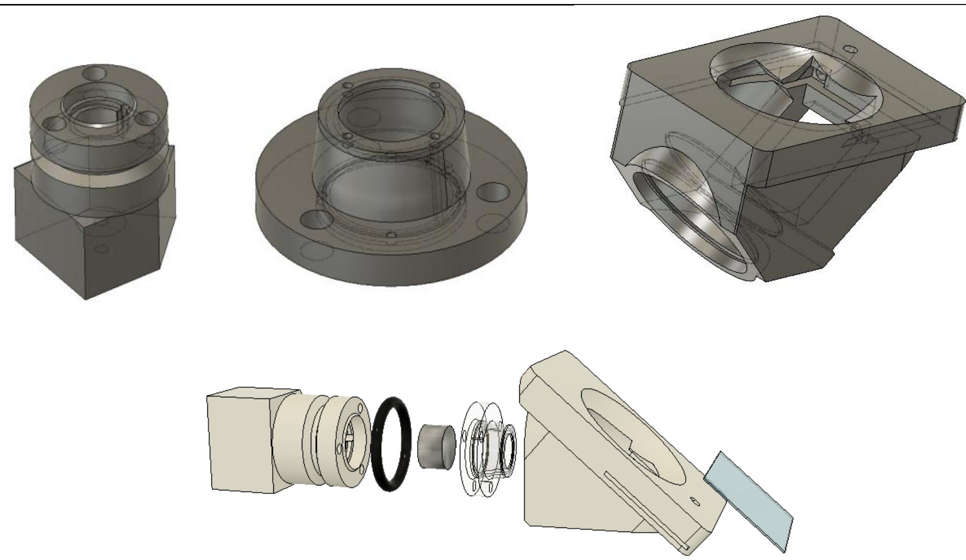

Figure 8: Newest revisions of CAD drawings of all three components. Upper left: transducer back; upper center: hollow focusing cone; upper right: experiment basin. Bottom exploded view shows, from left to right, the assembly arrangement of transducer back, nitrile O-ring, transducer crystal, focusing cone, basin, and glass slide.

I chose a collimator cone geometry from the output set with a simulated focal region radius of 2.8 mm and length of 6.5 mm. I fabricated each cone by 3D printing its CAD model with a resin stereolithography printer (Form 3, Formlabs, MA, USA) using XY- and Z-resolutions of 25 µm and 50 µm respectively. For each cone, seven of the eight vent holes were sealed with UV-cured printing resin; the final hole was sealed with flowable silicone. I fabricated the back casing of the transducer using the same printing parameters. A transducer (fundamental frequency = 200 kHz nominal; diameter = 10.0 mm) made of PZT material (DL-47, DeL Piezo Specialties, FL, USA) is mounted inside the transducer casing, soldered to a cable terminated by a micro-coaxial connector, and sealed with silicone. A nitrile O-ring is attached to the casing for a fluid-proof connection with the experiment basin, and acrylic cement is used to fix the cable to the resin body. I added metal threaded inserts and brass screws to connect the backing unit to the cone, and applied a layer of insulating tape to the exposed surface of each transducer. The finished collimator and transducer casing prints are pictured in Figure 9.

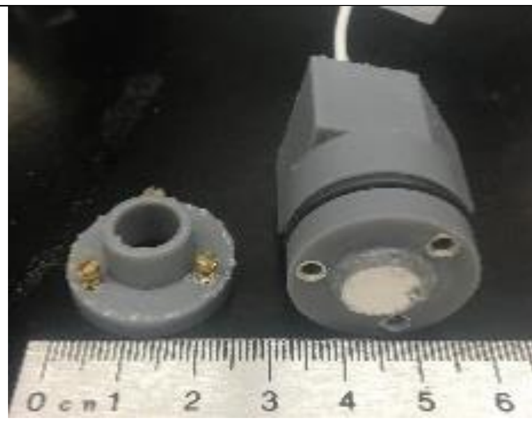

Figure 9: Completed fabrication of a transducer embedded in its custom backing component (right) and the hollow collimator cone (left).

This procedure was repeated three times to obtain units numbered NFHD-13 through -15. Units NFHD-13 through -15 were prototypes used to determine fabrication and calibration best-practices; a later series of experiment-quality units were denoted NFHD-016 through -019. Each unit was impedance-matched as close to 50 Ω as possible via external low-pass resonant matching networks, each measured using a vector network analyzer (VNA) (ZNL3: Rohde and Schwarz, Munich, Germany). The matching circuits were tuned to the individual resonant frequencies of the transducers, which were slightly different than the nominal 200 kHz. I performed various complementary inquiries on the prototype transducer units to investigate practical concerns such as the approximate expected conversion efficiency, the maximum applicable power before damage is incurred, the influence of an apparent heating effect, and whether various characteristics (e.g. electrical impedance and conversion efficiency) remain adequately stable over the operating range. For those that were not found to be stable, I attempted to determine the cause of the variation, and the variation was recorded and accounted for.

Cyclical improvement of the device design. I periodically revisited all parts of the above design procedures and fabrication procedures from 2018 until 2021, including after the design goals were adequately met. The simulation parameters and optimization parameters were occasionally adjusted, leading to re-generation of the set of optimum geometries; the 3D CAD models were frequently modified to add or improve features, such as the optical window in the basin; and it was necessary to change fabrication protocols across revisions – for example, the reflecting air gap was not properly 3D-printed in many revisions of the cone design, and the standard curing and finishing procedures proved incompatible with such a delicate physical feature.

First experimental validation of simulated fields. The production-quality unit NFHD-016 was mounted in a water tank alongside a 1 mm diameter needle hydrophone (NH1000, Precision Acoustics, UK) on a 3D positioning system (UMS3 Scanning Tank, Precision Acoustics, UK). The transducer was powered with 20 sinusoid pulses of 10 V_{pp} every 1 ms – corresponding to approximately 18.4 mW delivered electrical power – at its resonant frequency of 192.5 kHz, slightly under the nominal 200 kHz. The hydrophone was swept in 2D scans covering 20 mm by 20 mm in 1 mm steps in the plane perpendicular to the propagation direction, and I acquired five of these planar scans spaced 4 mm apart resulting in a final acquisition volume 20x20x16 mm. The pressure measurement at each voxel was the root-mean-square (RMS) value of the acquired hydrophone signal; by taking the RMS value over a time window in which the pressure is oscillating at its stable maximum, I can use RMS pressure as a proxy measurement of peak pressure that is more resistant against noise than directly measuring the peak.

To determine the position of the hydrophone measurement plane relative to the position of the device, I first attempted to use time-of-flight, but the precision of time-of-flight measurement is related to the ultrasound wavelength; for our chosen frequency, the wavelength in water is about 8 mm, so a precision of ±λ/2 or even ±λ/4 is insufficient for our purposes. Instead, a protocol using a leveled laser and rulers was used to determine the distance between the device and the hydrophone to a precision of ±0.5 mm; this is referred to as the pseudo-time-of-flight measurement. The field shape information obtained in this step was used to draw two targeting contours on the glass slide upon which the brain slices were mounted. The inner contour corresponds to the half-maximum intensity boundary, and the outer contour corresponds to the half-maximum pressure boundary.

Calibration of absolute pressure. I used two independent methods to measure the absolute magnitude of the pressure field emanating from our device. The first method measures the conversion efficiency of the device to establish a known number of total acoustic Watts transmitted, and then uses that quantity in conjunction with a wide-field scan to compute the absolute pressure within the focal region. The second method was to directly measure the pressure field using a calibrated hydrophone.

Radiation force measurements were performed to determine the efficiency of the ultrasound device using an analytical scale (PI-650, Denver Instruments, CO, USA) and an acoustic absorber for low-frequency emissions (custom-built; Precision Acoustics, Dorset, UK) using standard protocols described in [91]. Electrical power was measured with a power meter (N1914A, Agilent Technologies, CA, USA) and low-power coupler (BC-0060-10N, Universal Microwave Components Corporation, VA, USA). Preliminary testing indicated that the presence of the collimator did not significantly change the efficiency or impedance of the units, so all radiation force measurements were conducted without the collimator. I applied varying intensities of continuous-wave ultrasound signal at the resonant frequency; to limit the influence of transducer heating, the order of intensities was randomized, and the duration of continuous sonication was kept below 10 seconds. I used stimulus voltages of 0.4 to 1.1 V in 0.1 V increments, specified at the function generator prior to an RF attenuator with gain -20 dB and an RF amplifier (240DL, Electronics & Innovation Ltd., NY, USA) of constant nominal gain +50 dB; the -20 dB attenuator is installed for the protection of the amplifier. The procedure was repeated 3 times across each tested unit.

The same acoustic tank protocol as in "First experimental validation of simulated fields" was then repeated with a wider scanning field (40 mm by 40 mm), with the position of the plane as close as possible to the mouth of the collimator. I confirmed that the measurement points at the edge were at least 20 dB lower than the pressure at the center, corresponding to the assumption that the widefield scan encloses nearly all of the acoustic power. I can then calculate absolute (i.e., calibrated) pressure values for this setup by combining information from: (1) the integral summation of the recorded (non-calibrated) pressure values, (2) the radiation-force estimate of efficiency, and (3) the known forward electrical power during the widefield scan.

Similar procedures were repeated with a 0.5 mm calibrated needle hydrophone (HNR-0500: Onda Corporation, Sunnyvale, CA, USA); in an acoustic tank, the entire basin with the transducer installed was submerged and the transducer was stimulated with a sufficient number of pulses to reach steady-state. The calibrated hydrophone was positioned only at the spatial peak of the acoustic field and the stimulus voltage was varied to obtain an end-to-end calibration curve. The spatial peak was determined as the highest pressure that the brain slice would experience, via a very small planar scan approximately 1 mm from the glass slide. To add to this calibration battery, the same spatial-peak pressure versus input voltage curve was obtained for the condition with the glass slide removed, and once again with the transducer pulled back into the retraction position. Order of voltages was randomized for all tests.

In addition to both these calibration tests, I recorded changes to each transducer's electrical impedance over applied power, which I found to change significantly across the operating range. This variation was unexpected for this matching method and surrounding system, but easily measured and accounted for. This is an important component to be able to properly predict delivered electrical Watts, and thereby use the radiation force calibration data; however, the calibrated hydrophone data sidesteps this requirement because it is calibrated against acoustic energy directly.

System implementation. An easy-to-use software console was developed and installed on the lab computer to program instrumentation using NI-VISA communication libraries. The console was developed concurrently with frequent user consultations, engaging the experimenter who was primarily responsible for conducting the experiments of Chapter 3 (C. Swytink-Binnema); evaluating for usability among a diverse group of users was not prioritized, as we foresaw only one user in the short term. The software console includes a feature to determine the electrical settings required to deliver a given acoustic dosage. It also interfaces with the power meter to verify and log the delivered electrical power on each sonication. A screen-capture of the console interface is shown in Figure 10. The Python code and list of dependencies for the console is hosted at https://github.com/ProteusMRIgHIFU/NFHD_Console.

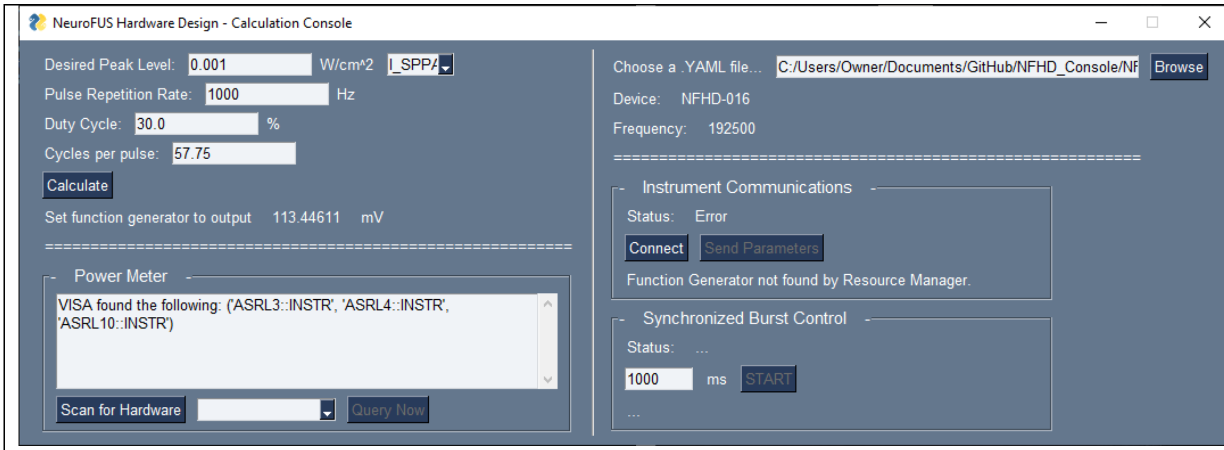

Figure 10: Screen-capture of version 1.0 of the console for programming and conducting LIFU experiments. The console communicates with instrumentation to send the desired timing sequence, and communicates with a power meter to verify the delivered acoustic dose.

Two electrical signal generators (Agilent 33521A and 33522A) were programmed such that one produced rectangular pulses according to the kHz-range pulse repetition rate, and the other produced the sinusoidal driving signal at ultrasound frequency. The two were arranged such that the rectangular pulses were used to gate the output of the ultrasound driving signal. The output of the ultrasound driving signal generator was attached to an RF attenuator with gain -20 dB and an RF amplifier (240DL, Electronics &Innovation Ltd., NY, USA) with nominal gain +50 dB; the output of the RF amplifier was connected through the power meter low-power coupler to the matching box assembly for the transducer. To achieve synchronization with the electrophysiology setup, the pulse-gating function generator was externally triggered by a digital output port on the digitizer (Axon Digidata 1440A: Molecular Devices, San Jose, CA, USA). The digitizer was controlled and programmed by the Clampex software console (Molecular Devices, San Jose, CA, USA), also running on the lab PC. Figure 11 below shows a flowchart diagram of these connections comprising the system I assembled to validate the ultrasound system (and later to conduct brain slice experiments). The green and amber flowchart elements in Figure 11 correspond to the connections mentioned in this paragraph, and the blue elements correspond to electrophysiological recording equipment that we had limited ability to modify.

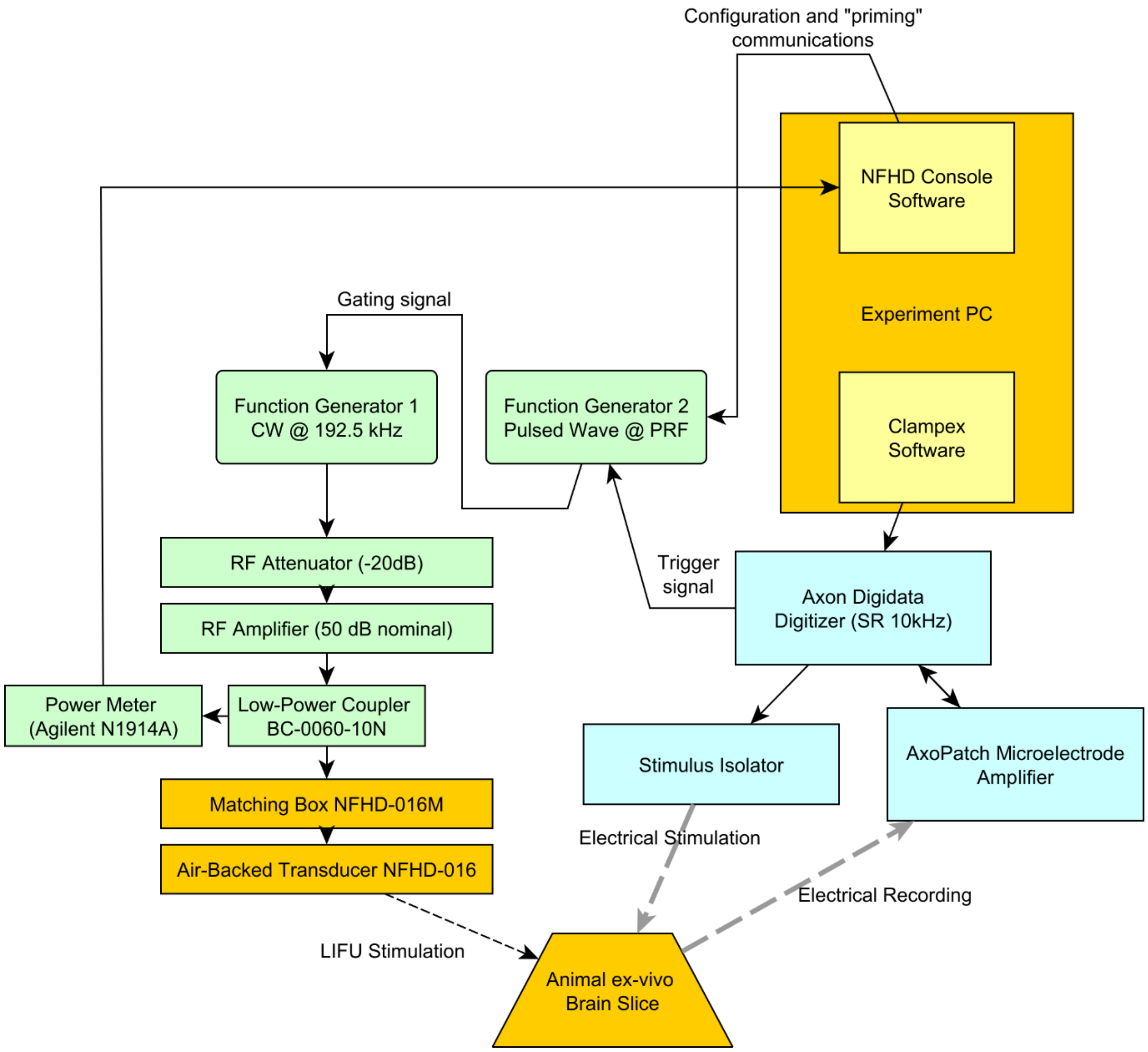

Figure 11: Flowchart showing the connections between elements of the experiment platform. Note the connecting arrow labelled "Trigger signal," the electrical signal facilitating synchronization between the electrophysiological recording equipment and the ultrasound system.

2.4: Results

Fabrication. Table 2 below contains the exact operating frequencies for each transducer unit, determined after matching, and the radiation-force (lossy) estimates of efficiency. NFHD-017 was damaged before being calibrated, and is omitted from the table.

Name	Status	Operating Frequency (kHz)	Efficiency (%)
NFHD-012	Prototype	191.0	-
NFHD-013	Prototype	196.0	3.2
NFHD-014	Prototype	187.0	2.2
NFHD-015	Prototype	189.0	2.0
NFHD-016	Production-quality	192.5	3.2
NFHD-018	Production-quality	192.6	-
NFHD-019	Production-quality	194.8	-

Table 2: Summary of characteristics for fabricated transducer units, post-matching.

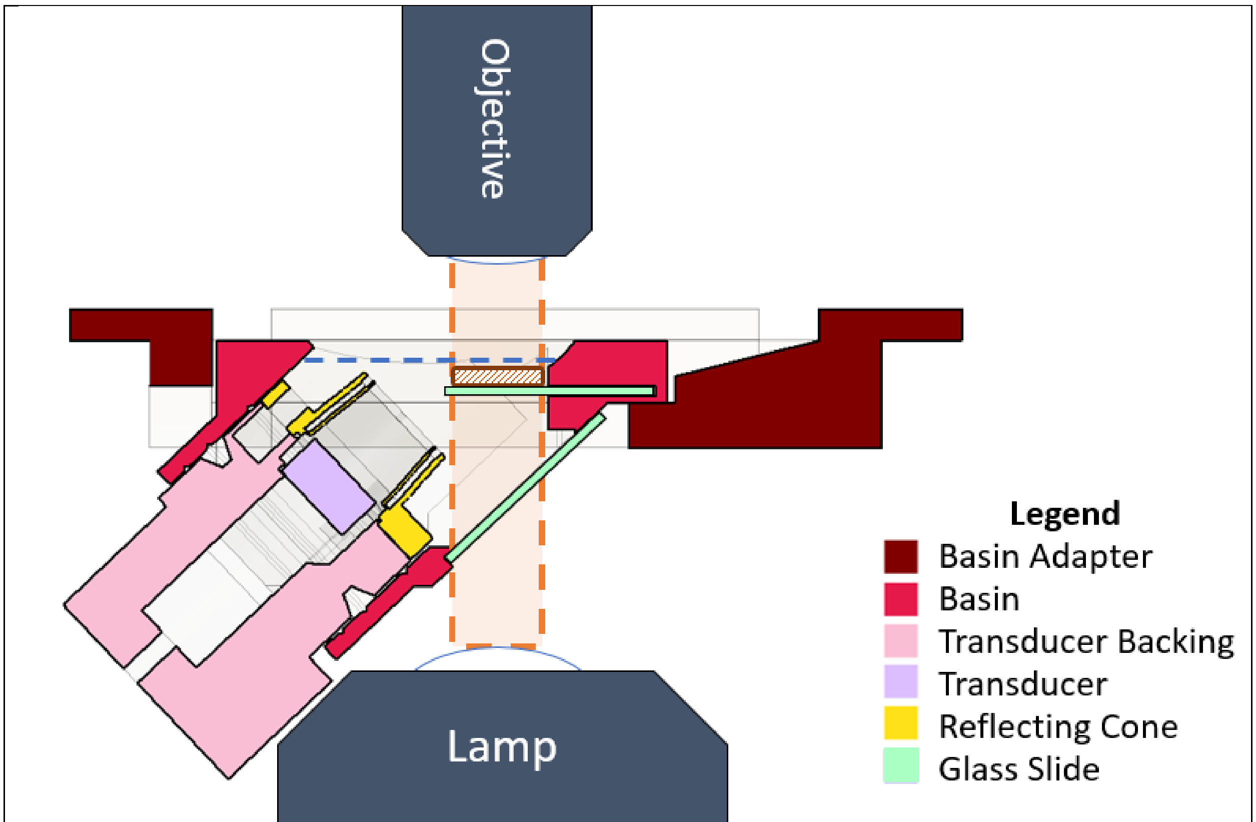

Figure 12: Schematic diagram of the LIFU system hardware components installed in the microscope platform. As in Figure 4, the orange dashed zone represents the necessary line-of-sight, and the dashed blue line denotes the fluid domain (the surface level of the ACSF that sustains the brain slice).

First experimental validation of simulated fields. Figure 13 below shows the measured 3D field emanating from unit NFHD-016 with focusing cone attached; it is compared against the normalized simulated field using the pseudo-time-of-flight measurement.

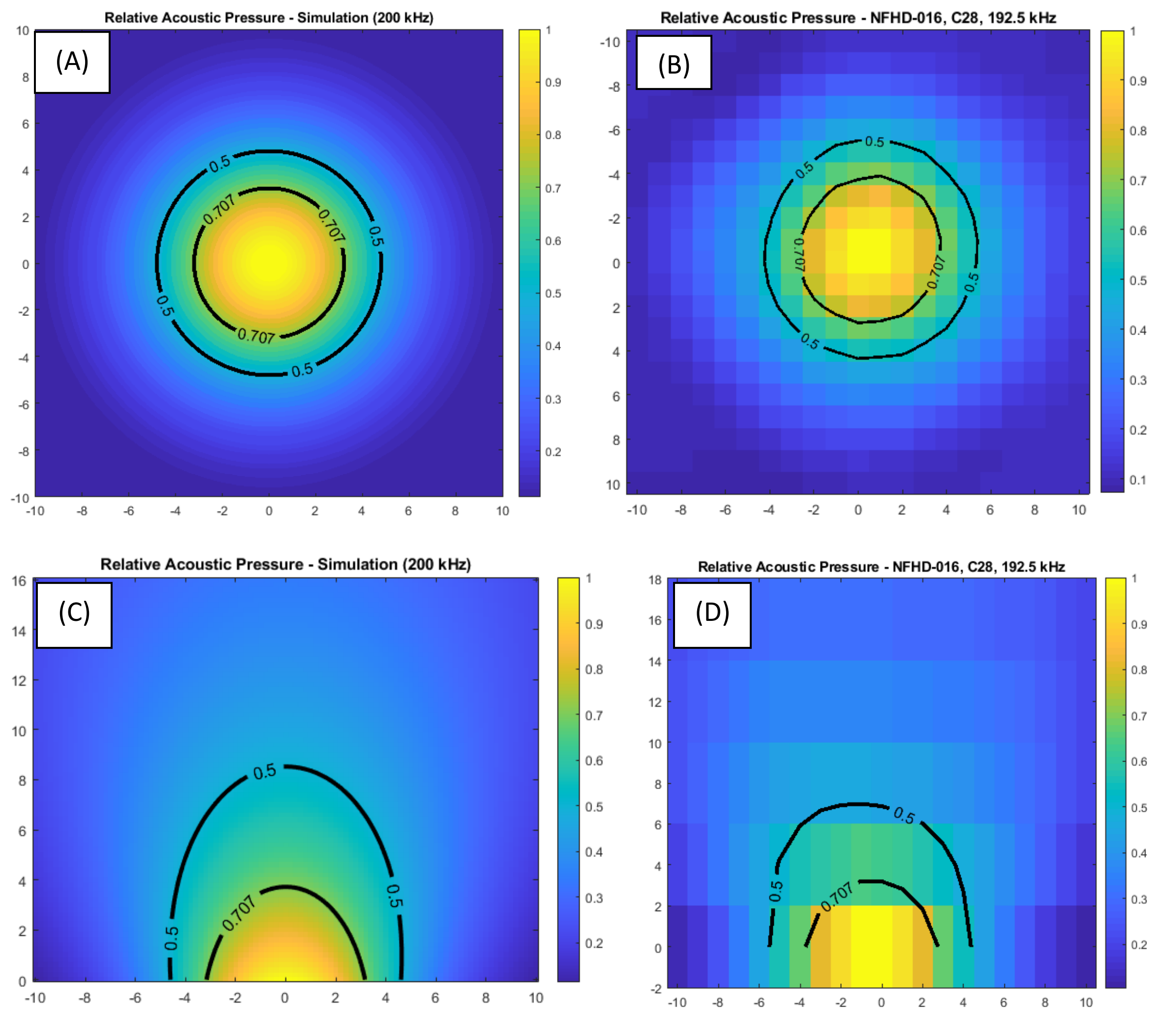

Figure 13: Comparison of simulated pressure field (A and C) and 3D field scan (B and D). (A and B) are in the plane parallel to the transducer surface, and (C and D) are perpendicular to the transducer surface. Z=0 (0 on the vertical axis of C and D, and the entire plane of A and B) is located 14.2 ± 0.5 mm from the transducer surface. All axes are in mm.

Figure 14: Targeting contours on the glass slide, drawn based on 3D field shape measurements.

Calibration of absolute pressure via radiation force method. Using the power meter and low-power coupler, I determined that the electrical power delivered by our widefield test sequence was 18.4 mW, converted to a total acoustic forward power of 0.59 mW for unit NFHD-016 (3.2% efficiency measured by radiation force on scale; see Figure 15). Applying the assumption that the 40 mm by 40 mm widefield scan captured virtually all of the acoustic energy, I calculate the conversion from non-calibrated hydrophone voltage units to Pascals. From there, I assume that sound intensity is linear with delivered electrical power to obtain the conversion factor from delivered mW to I_{SPPA} in the plane parallel to the transducer surface (and offset by the distance to the brain slice). For NFHD-016 this conversion factor was 0.0276 mW/(W·cm^2) = 0.276 m^{-2}.

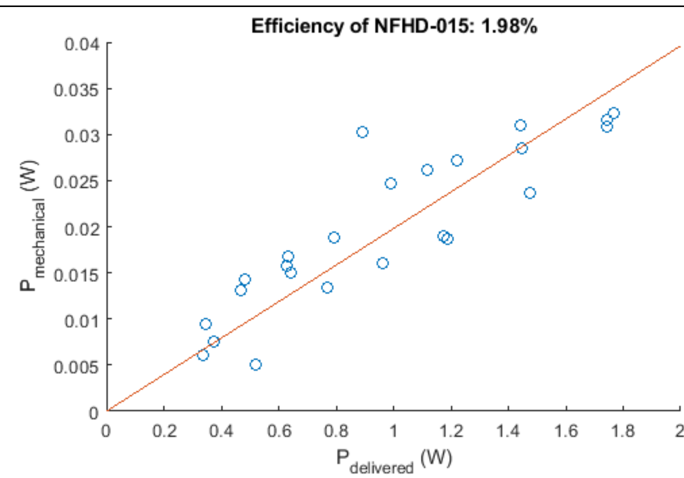

Figure 15: Sample calculation of efficiency via regression for a single unit.

The curve in Figure 16 shows variation in electrical impedance over the power range.

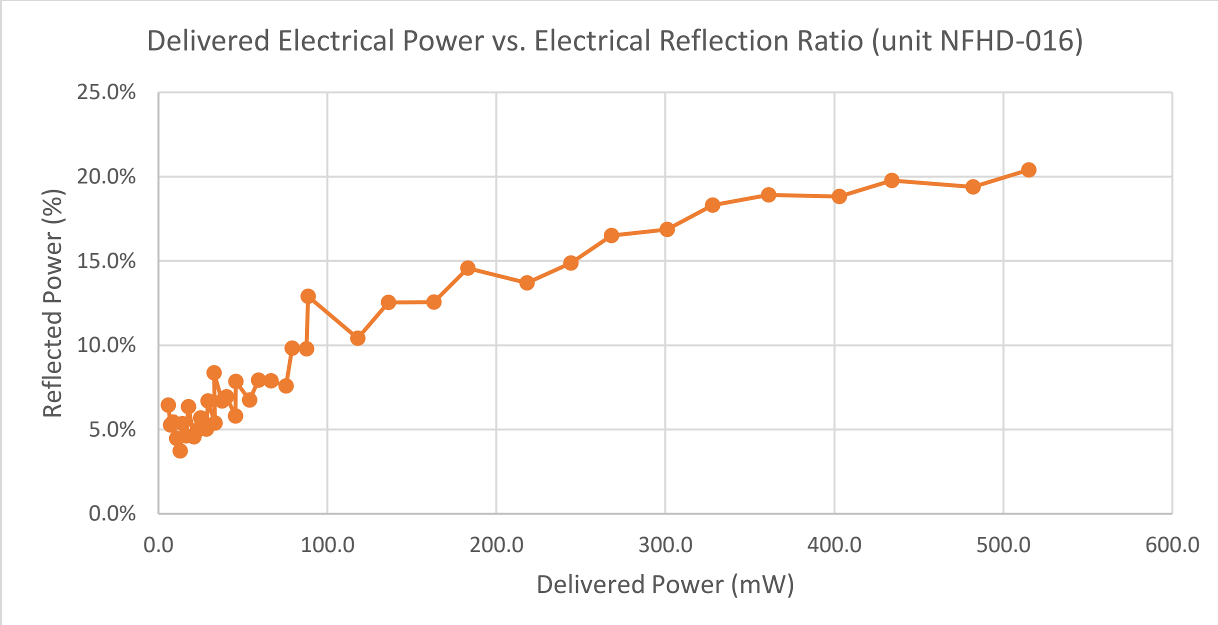

Figure 16: Relationship between applied electrical power and ratio of that power which is reflected. This indicates a change in the electrical impedance of the device over its operating range.

Calibration of absolute pressure via calibrated hydrophone. The following spatial-peak pressures were recorded using the calibrated hydrophone; the corresponding estimates of peak pressure value using the radiation force estimation method are overlaid on the same plot.

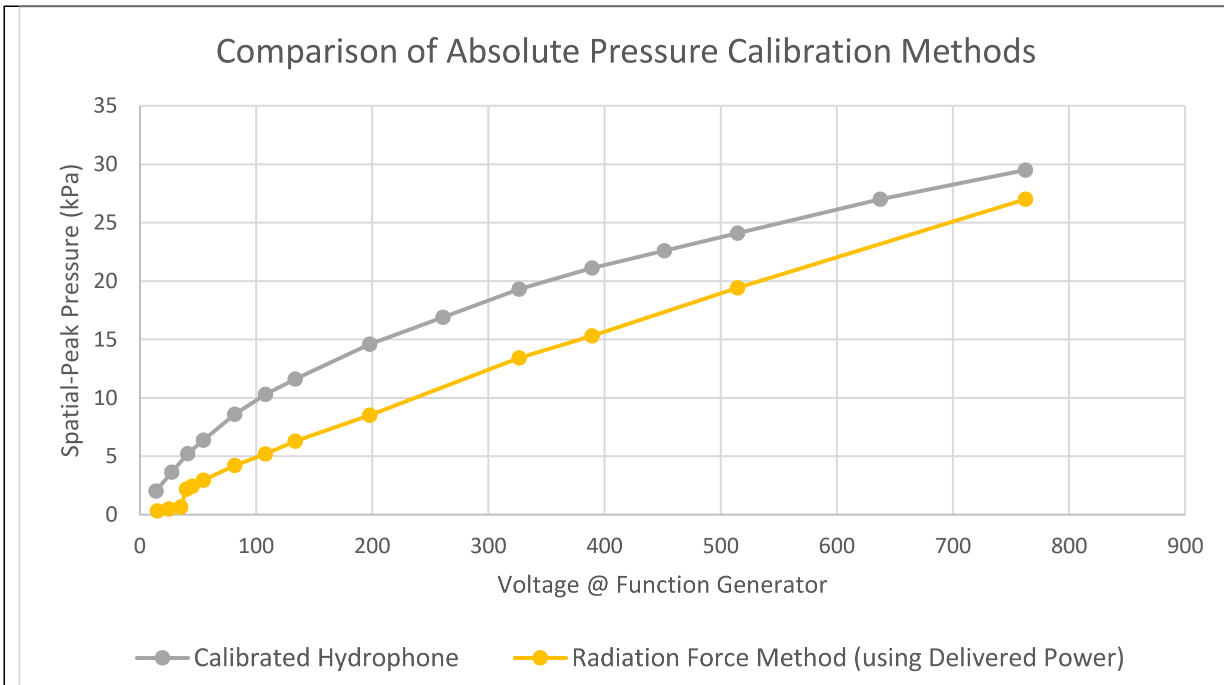

Figure 17: Comparison between the two methods of obtaining absolute pressure values. The calibrated hydrophone data (gray line) is the more accurate measure.

The underestimation is expected because both the wide-field scan and the radiation force methods are lossy. The magnitude of the underestimation is smallest at high delivered powers (8% difference) but as large as 55% difference at low and medium powers. Note that because acoustic intensity is proportional to the square of acoustic pressure, this result suggests that the radiation force method can underestimate peak intensity by a factor of up to 4.

The relationship between applied voltage and peak acoustic pressure is nominally linear, but the curved shape of the trend in hydrophone measurements of pressure is still somewhat expected; it resembles the observed trend in change of electrical impedance (shown in Figure 16), which corresponds to electrical and therefore acoustic power delivery.

2.5: Discussion

Design Goals: Performance and Compatibility. There was one noticeable discrepancy with chosen performance goals: the acoustic focal region of the chosen geometry originally bore a radius of 2.8 mm, but the focal contour on the glass slide has an approximate radius of 4.5 mm. This is a consequence of evaluating each pressure field normalized to a maximum value that was positioned very close to the mouth of the collimator – that is to say, normalized to a maximum value that the target would not experience. The orientation of the setup is such that there is about 5 mm of room between the tip of the collimator cone (which was the beginning of the region under consideration during design) and the edge of the brain slice in the basin. Regardless, when the actual distance between the device and the sample is properly accounted for, there is very close agreement between simulation and measurement (see Figure 13); the discrepancy is only with the chosen performance goals.

In terms of compatibility, every goal was met as of the latest revisions except one: a persistent stimulation artifact at the pulse repetition frequency that was detected by the electrophysiology setup coinciding with ultrasound stimulation. I hypothesize that this artifact arises due to capacitive coupling between the transducer surface and the measurement elements, but it proved challenging to conclusively characterize. Ultimately, we resolved to account for this by implementing as many systematic controls as possible during later phases of experimentation.

Alternate formulations of cost function. Slight changes to the cost function could influence the set of yielded designs. One valid modification might involve manual interpolation of the focal region instead of offloading to MATLAB's algorithm, or similarly querying COMSOL for the contour directly (the current workflow interpolates once to obtain values from the finite-element mesh, then interpolates again once the values are imported into MATLAB, which is unnecessary). More dramatic changes could instead involve different measures for determining focality: for example, the rate at which pressure decays outside the focal region may be a more useful measure of targeting selectivity; similarly, optimizing for the greatest ratio of energy in-focus to out-of-focus is a viable alternative. Another modification would take into account that acoustic intensity is defined for a certain plane; I could have worked in terms of the intensity experienced in the plane of the brain slice, or any other plane determined to be neurophysiologically relevant. However, there is currently insufficient mechanistic context to inform these choices.

Adding certain additional realistic constraints to the FEM simulation could have incurred a tradeoff between speed of evaluation and accuracy. One example of a condition that could be directly added to the 2D model with a small cost to evaluation time is incorporating acoustic-solid interaction with the resin casing. Examples of conditions that would require switching to 3D and would thus incur a more significant cost to evaluation time are: acoustic-solid interaction with the glass slide and the walls of the basin; modeling reflections off the top surface of the ACSF. In a similar vein to these last modifications, we considered exploring non-axisymmetric geometries for the collimator; this concept would have reduced performance both in terms of the 3D evaluation and in the complexity added to the optimization space.

It may have been feasible to add additional degrees of flexibility to the finite element model without disrupting the iterative design workflow. Specifically, the position of the contiguous reflecting elements relative to the transducer could have been incorporated as 1 or 2 additional degrees of freedom; for a range of about 0-3 mm in each direction, this would have still been amenable to the existing hardware design, and would have increased the diversity of shapes generated. However, transducer-specific characteristics of thickness (i.e. fundamental resonant frequency) and diameter are *not* as reasonable to be incorporated as degrees of freedom, for two reasons: first, that they would violate fair comparison – for any range of frequencies allowed to optimize over, the physics cause the highest frequency to be favoured; second, that varying those parameters would incur significant extra cost in terms of ordering many batches of transducers with different specifications, and significant inconvenience in terms of needing many revisions of every physical part for each set of transducer dimensions (by contrast, the current setup varies only the collimator cone). This is related to our decision to choose transducer diameter and thickness values at the beginning of investigations.

Misalignments in the acoustic tank. It is challenging to ensure that the movement axes of the 3-axis positioning system are aligned with the transducer and transducer housing. This leads to data typically being captured a few degrees off-axis relative to the true central axis of the ultrasound device. To try and rectify this, I developed a script to find the true central axis using independent component analysis (effectively a 3D linear regression), and then rotate captured data as though it was recorded perfectly in-axis. However, this approach has a major weakness: it disguises any misalignments arising from asymmetries in the manufacture of the transducer or collimator. Strategies involving use of time-of-flight to correct this misalignment bear the same weakness discussed earlier: that the precision is based on the wavelength, and the wavelength is too long at 200 kHz to make accurate corrections. To establish a better spatial ground truth, one viable approach would be to mount a distance-sensing apparatus into the hydrophone holder (e.g., a laser distance sensor, a mechanical actuator, or a high-frequency ultrasound probe) and move it along the axes of the 3-axis positioning system to verify the alignment of the transducer mount.

2.6: Conclusion

I successfully built and tested a system to enable experiments studying the effects of focused ultrasound on electrical activity in acute brain slices. My development process led to computer-optimized hardware geometries; both the optimization procedure and the air pocket reflector itself are viable innovations in experimental ultrasound hardware design. The reflecting acoustic collimator concept appears to be a promising alternative to refractive waveguides, and I confirmed it to be compatible with our space-restricted experimental platform. The tools, techniques, and strategies described in this chapter constitute a useful starting point for future refinements of this platform or development of similar systems by our laboratory.

3. Replicability Study: Ultrasound-Induced Modulation of *in vitro* Evoked Local Field Potentials

Jak Loree-Spacek,[a] Catherine Swytink-Binnema,[a] Zelma Kiss,[b] Laura Curiel,[c] Samuel Pichardo[d]

[a] Biomedical Engineering Graduate Program, University of Calgary, Calgary, Canada
[b] Dept of Clinical Neurosciences, Cumming School of Medicine, Calgary, Canada
[c] Dept of Electrical and Computer Engineering, Schulich School of Engineering, Calgary, Canada
[d] Depts of Radiology and Clinical Neurosciences, Cumming School of Medicine, Calgary, Canada

3.1: Abstract

In this communication, we present results demonstrating the successful implementation of the experiment system described in the previous research chapter. We applied pulsed low-intensity focused ultrasound (LIFU) sequences to acute rat brain slices with simultaneous electrophysiological recordings and assessed LIFU-induced changes to evoked local field potentials (LFPs). Our study primarily sought to establish the replicability of observed modulation effects. LIFU-induced modulation of electrical activity was observed in 57% of brain slices (25 of 44) for which a recording could be obtained. We conducted a battery of control tests to ensure the elicited effects were not excessively affected by spurious factors such as vibrations along the mounting slide or electrical interference. It was later determined that one unanticipated confound persisted, and likely dominated any interactions between ultrasound and endogenous mechanisms. We addressed and eliminated the confound by the end of the thesis work, but it is present in all the results shown here. Despite the influence of this confound, the experiment platform is considered functionally validated moving forward.

3.2: Introduction

Background. We discovered from preliminary testing that we could elicit ultrasound-induced modulation of evoked LFPs in acute rat brain slices with moderate consistency. We used the custom basin and transducer assembly whose development I described in the previous chapter.

Objectives of this study.

1. In preparation for our labs' upcoming studies of mechanisms and effective parameters, I aimed to fully validate my novel hardware system within the experiments for which it was designed.

2. We would like to determine the success rate of modulation effects that we observe so that we have proper expectations for this experimental system and this particular model organism. This facilitates appropriate choice of sample sizes in later series of experiments.

Ultrasound parameters. A rectangular-pulsed ultrasound stimulation sequence can be characterized in terms of fundamental frequency (f_0), pulse repetition frequency (PRF), duty cycle (DC), and an intensity measure (P_{peak}, I_{SPTA}, or I_{SPPA}); as I described in more detail in Chapter 1, the influence of these parameters is mostly varied and unclear across studies. However, across numerous model organisms and electrophysiological indicators, literature consistently reports an intensity-dependent effect. As a result, we decided to use fixed timing parameters (f_0, PRF, DC) and vary only ultrasound intensity for the sake of this replicability study.

3.3: Methods

1. Replicability study. We used a Vibratome (VT1000S, Leica Instruments, USA) to produce 350-micron thick coronal brain slices from encephalectomized rats. The brain slices were incubated for 90 minutes in 30-degree Celsius artificial cerebrospinal fluid (ACSF) bubbled through with carbogen. Glass electrodes were prepared for the electrophysiology setup and filled with 3 M KCl. Each brain slice, either a hippocampal or cortical slice, was positioned on the glass slide within the basin at the center of the concentric targeting reticle. For hippocampal samples, the recording and stimulating electrodes were inserted into the CA1 region; the tip of the recording electrode was oriented in the stratum radiatum and the stimulating electrode was inserted a few millimetres upstream. For cortical samples, the recording electrode was positioned in layer 2/3 and the stimulating electrode was positioned in layer 4.

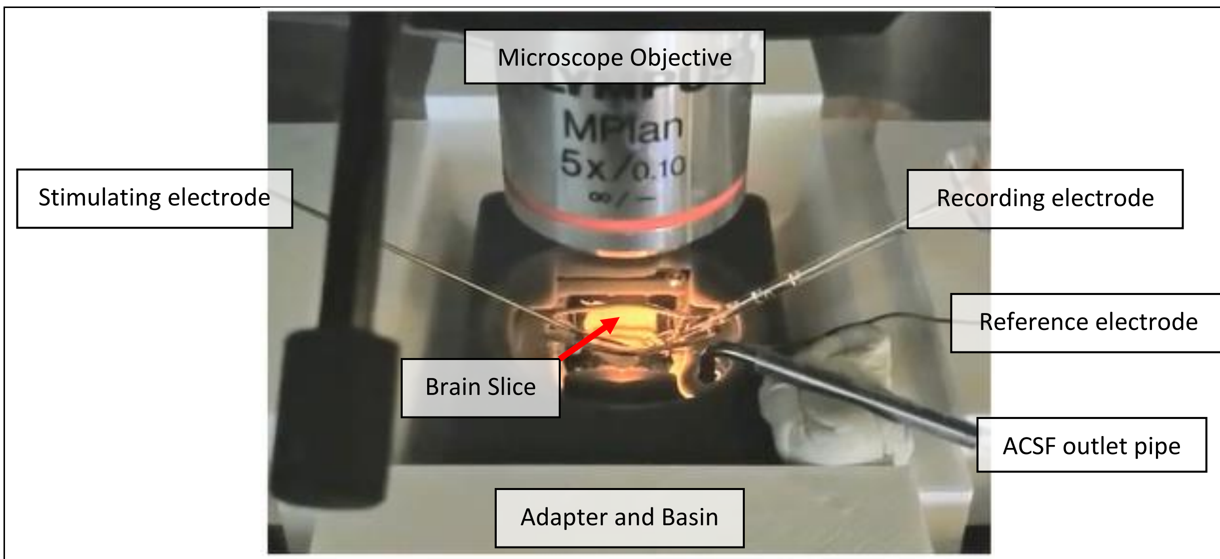

Figure 18: Photo of the stimulating and recording electrodes inserted into a rat brain slice.

Slices were subjected to electrical stimulation in the form of a 0.2 ms current pulse every 4.0 seconds. Each LIFU sequence consisted of 5 successive 4-second sweeps in which we applied pulsed 192.5 kHz ultrasound, synchronized to begin 1010 ms before the electrical stimulation pulse and end 510 ms before the electrical stimulation. The LIFU was pulsed with 30% duty cycle and 500 Hz pulse repetition rate. For each slice sample, we applied ultrasound intensities from I_{SPPA} = 0.26 mW/cm^2 increasing monotonically to I_{SPPA} = 128 mW/cm^2 in linearly spaced steps. We developed this protocol using preliminary results to choose the sequence parameters that led to the most reliable observation of this effect; the 510 ms spacing between the end of ultrasound exposure and the beginning of the electrical pulse was the shortest duration that did not cause instability artifacts in the recording system. Figures 20A & 20B show this protocol in the form of timing diagrams.

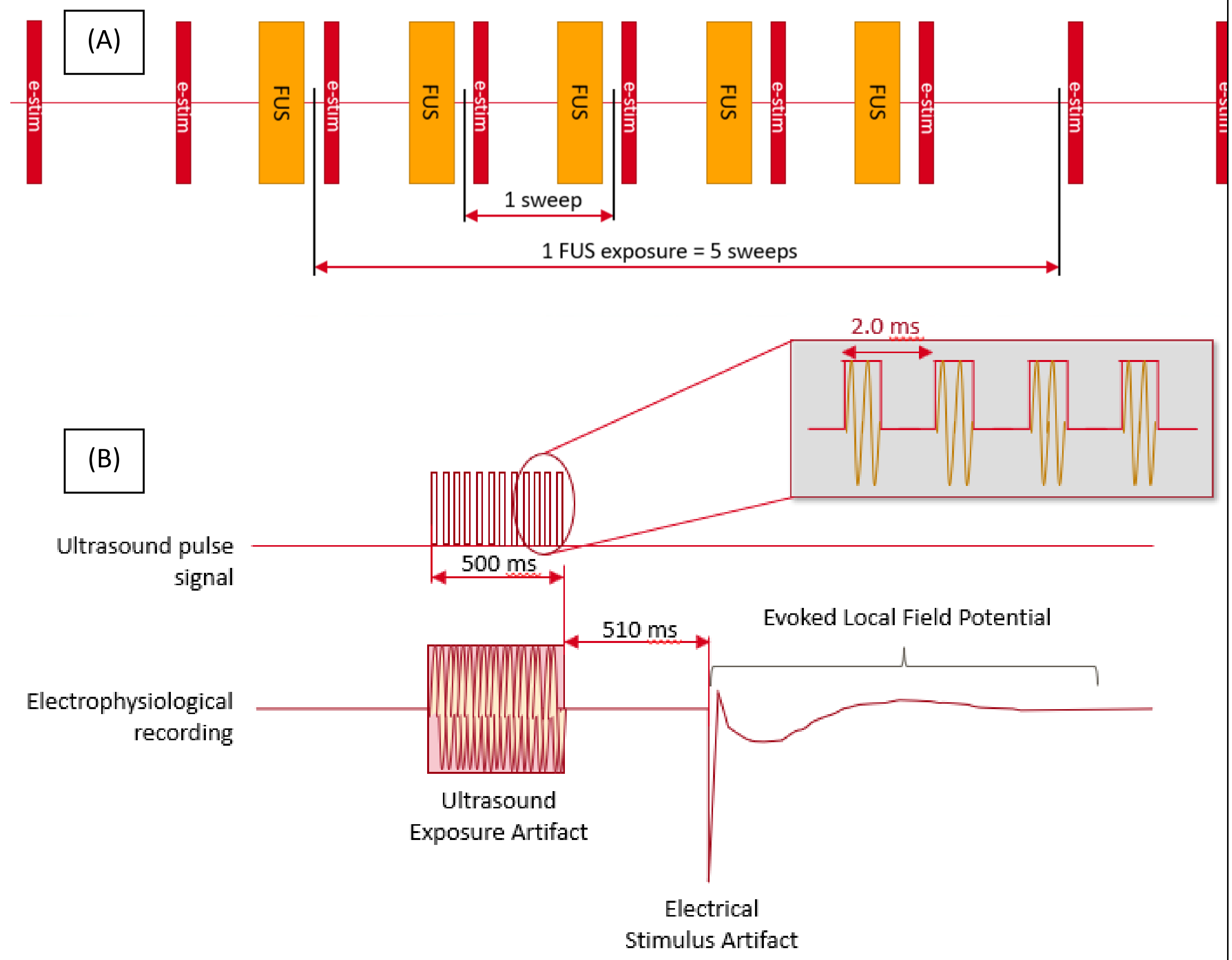

Figure 19 (A): Timing diagram showing the arrangement of repeated electrical stimulations and interleaved blocks of ultrasound application within one LIFU sequence. We waited 10 minutes between exposures to allow the evoked LFP to return to baseline. (B): Timing diagram showing arrangement of protocol features within a single sweep.

We waited 10 minutes between successive LIFU stimulation sequences. Upon observing a significant change to the evoked LFP, the sample was deemed successfully modulated; if the maximum ultrasound intensity was reached with no change to the electrical response, the sample was deemed unresponsive. Examples of responses that constituted a modulation effect are described in the Results section. Brain slice samples for which a stable evoked LFP response could not be established were discarded, and not tallied as either successful or unsuccessful.

2. Establishing controls. We investigated two factors to ascertain whether they interfered with or confounded the results from this setup. A third confounding factor emerged after we obtained our results; it is discussed briefly here, and then in further detail in Section *3.4: Results*.

Sham FUS condition. For a slice in which a reliable modulation effect was established, a sham test was conducted by placing an air-gap barrier between the collimator and the brain slice. This obstacle to ultrasound (but not to direct electrical conduction) was intended to control for most forms of spurious electrical coupling between the transducer device and the brain slice sample. To account for minor mechanical disruption of the setup by the installation and removal of this barrier, we alternated (unimpeded FUS, then sham FUS, then unimpeded FUS) and attempted to verify that the modulation was observed on the FUS exposures and not on the sham exposures. We performed this procedure on three brain slices (two hippocampal, one cortical), with trials spaced by 10 minutes.

No glass condition. The glass slide that the slice sits upon has some relevance: although it is thinner than the ultrasound wavelength (thickness = 1 mm vs $\lambda \approx 7.5$ mm), it may contribute to slight distortion of the ultrasound pressure field. This is demonstrated by a finite-element simulation in which the acoustic-solid interaction with Pyrex glass is modelled (Figure 20). Additionally, the glass slide experiences different modes of physical vibration which may then be conducted to the sample in a different manner than the neural tissue would experience within its native extracellular matrix. Other studies have investigated the influence of spurious physical vibrations conducted through necessary solid elements of the measurement system [72]. Note that this solid substrate could not be feasibly incorporated into the original optimization design, as it cannot be modeled in a rotationally-symmetric manner, and the acoustic-solid interaction is also computationally taxing; the computation time for the 3D model shown in Figure 20 was approximately 45 minutes, and the computation time for the 2D-axisymmetric models in the optimization procedure was approximately 5-8 seconds. We modified the experiment basin to seat the brain slices on a nylon mesh (Figure 21) and attempted to obtain a comparable ultrasound-induced modulation effect in 3 brain slices. Calibrated hydrophone measurements positioned at the spatial-peak of the ultrasound beam demonstrated that the peak pressure experienced by the brain slice is very similar whether it is seated on glass or on mesh (see Figure 22).

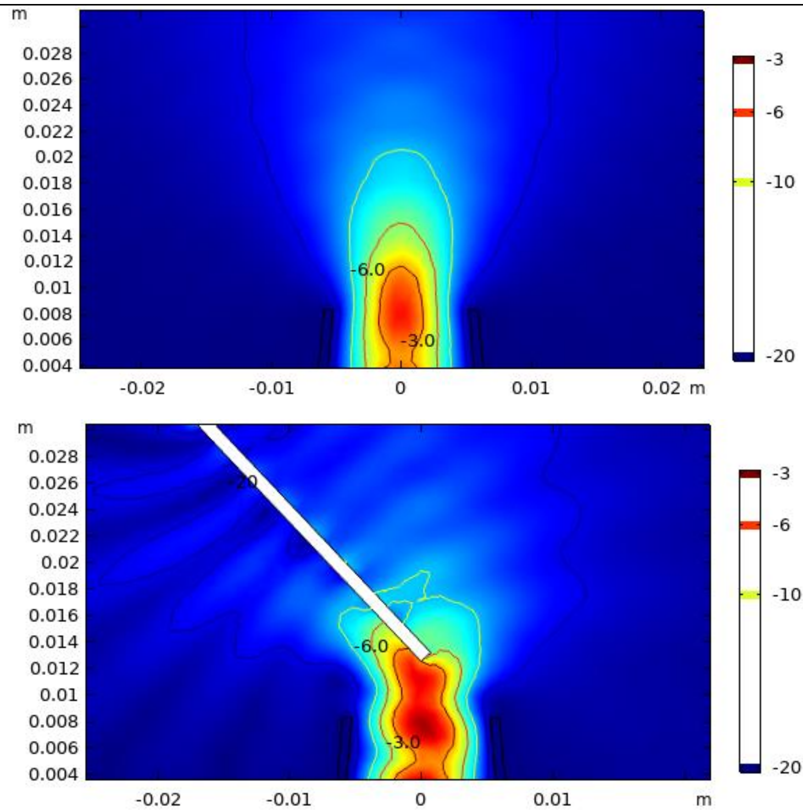

Figure 20: FEM simulation of normalized pressure demonstrating the slight distortion effect of glass slide presence. Transducer is a disc with 5mm diameter centered at x = 0 and pointing up.

Figure 21: Photo of mesh-pinned basin variant.

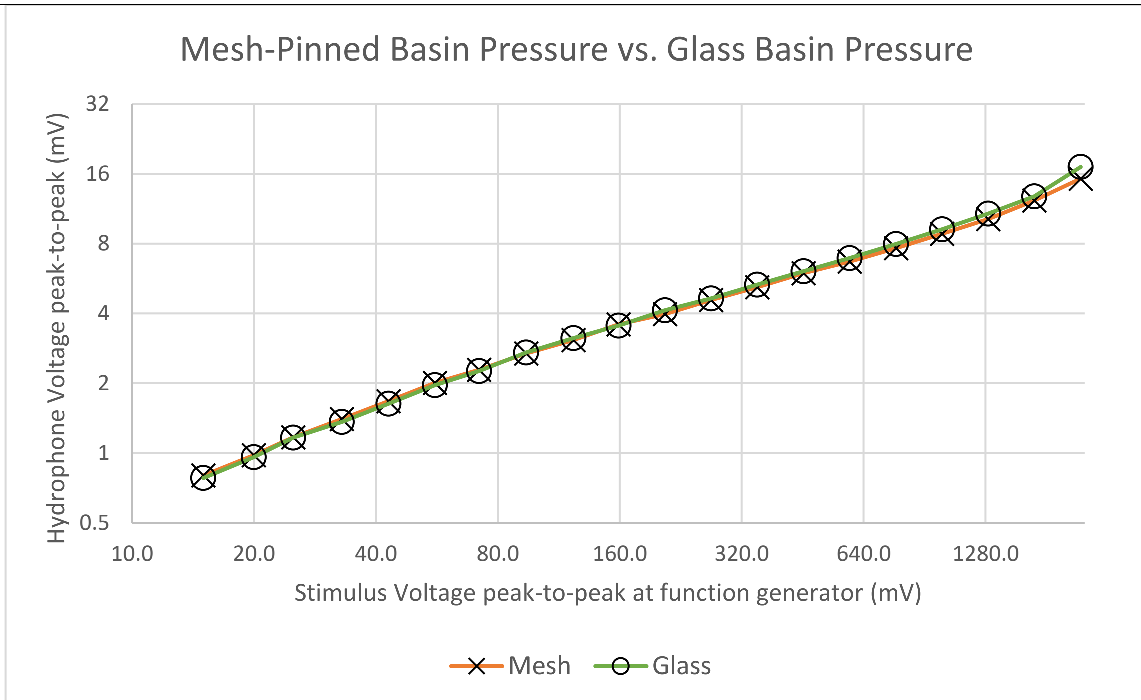

Figure 22: Comparison of calibrated hydrophone measurements of spatial-peak pressure on the glass & in the mesh-pinned basin. Each point is an average of 2 measurements with order randomized. Methods for measuring this pressure with hydrophone are detailed in Chapter 2.

Microfluidics confound. There are several features of the experimental setup and model organism that are different from how ultrasound would encounter brain tissue in a transcranial or *in vivo* setting, such as the glass slide substrate that was discussed. Some other setup properties that are difficult to control for are: the physical presence of two solid extracellular electrodes, which may disrupt or damage tissues, or which may be disturbed by ultrasound; the electrical presence of the recording electrode, which is minimized by the recording amplifier design and architecture, but which is nonzero nonetheless; and the damage inflicted upon the brain sample by the process of slicing it in the microtome, which can change the cellular, molecular, and neural circuity conditions of the sample. We designed control conditions to account for some of these features of the setup, at least in the context of their influence on the LIFU stimulation sequence. To investigate whether the electrical or physical presence of the recording electrode was confounding the effects of ultrasound, we extracted the recording electrode before sonicating and then replaced it in the same position after sonication. This was conducted in a slice that was known to display the modulation effect reliably, and using a LIFU sequence that was known to induce this effect reliably. Disturbingly, these preliminary experiments suggested that when the recording electrode was retracted for the duration of sonication, the modulation effect was not visible when the recording electrode was re-inserted.

Based on this initial finding, the primary investigator conducting these experiments (C. Swytink-Binnema) devised a follow-up experiment to test the hypothesis that LIFU stimulation was disrupting the KCl contained in the glass micropipette recording tip. When the KCl was replaced with food colouring solution, the food colouring solution was found to remain confined within the micropipette tip; however, when we applied a pulsed ultrasound sequence following the specifications of this study, the food colouring could be seen leaking into the surrounding brain slice through the microscope. This finding strongly suggested that, upon exposure to LIFU, concentrated KCl was being introduced to the brain sample at the recording site, likely causing an undesired chemical modulation of brain activity. In future experiments, we transitioned to metal electrodes, which are not susceptible to this interaction; however, all data in this chapter are subject to this microfluidic confound. The significance of this confound in the context of this replicability study is further addressed in Section 3.5: Discussion.

3.4: Results

1. Replicability study. The LFP modulation effect which we detected and chose to examine exhibited the following characteristics:

1. The modulation effect constitutes a transient decrease in the magnitude of the evoked LFP.
    a. On each sweep, the raw readout from the electrophysiology setup would feature, in chronological order: if the ultrasound exposure occurred, an unreadable segment for the duration of the ultrasound stimulation; a large negative deflection corresponding to the electrical stimulus used to induce the field potential response; and the LFP itself, a negative deflection of 0.5-5 mV lasting 10-50 ms after the electrical stimulus. The modulation effect would constitute a visually-distinguishable change to the shape and/or a decrease in the magnitude of the LFP response.
2. The LFP returns to its baseline shape after a few minutes.
    a. In hippocampal brain slices, evoked LFPs are often divided into the characteristic portions of fiber volley, population spike, and field excitatory post-synaptic potential (fEPSP), each with distinct neurophysiological underpinnings [92]; fEPSP slope is a measure of hippocampal evoked potential size that is less affected by noise and other features of the response. Measuring the fEPSP slope over time, the time constant of the modulation effect (i.e. time to return to 63.2% of the original value, relative to the

maximum change in the fEPSP slope) was found to be approximately 120 seconds when the applied ultrasound intensity was 0.55 mW/cm^2 I_{SPTA}.

3. The modulation effect was found to be intensity-dependent; some brain slices only responded when the intensity was increased beyond a certain level. Additionally, a higher intensity would typically correspond to a longer time to return to baseline, and occasionally a higher intensity would also correspond to a greater change in LFP amplitude as described in (1a.). The exact nature of the relationship with intensity is beyond the scope of this chapter and will not be further detailed here.
4. If the modulation effect is observed once in a brain slice at a particular intensity, that slice will continue to be responsive with near-100% success rate at that intensity over its 2-5 hour lifetime. That is to say, the modulation effect was found to be perfectly replicable within each slice.

Of the 44 brain slices tested between March 2021 and August 2021 within which a usable LFP response could be established, 25 (57%) displayed a modulation effect of the type described above. The remainder showed no change in LFP shape at any intensity level tested.

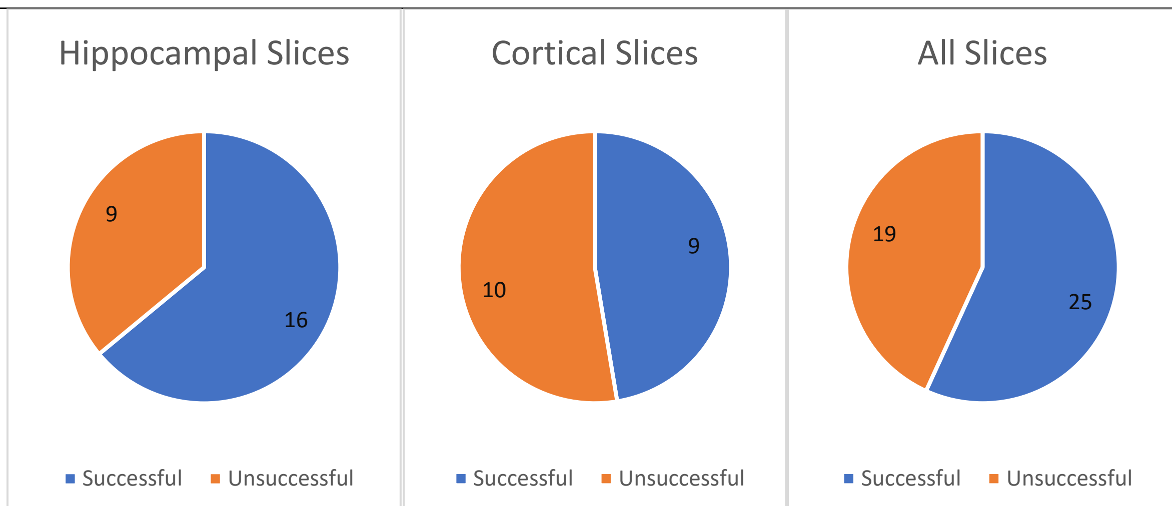

Figure 23: Success rates of all brain slices for which LFPs were recordable.

2. Establishing controls.

Sham FUS Condition. In all 3 slices that were selected for this condition, the response to sham LIFU closely resembled the baseline trace (i.e. no modulation), while the response to unimpeded LIFU resembled the successful modulation condition.

No glass condition. Of four hippocampal slices suspended on the mesh surface in October 2021, three showed a successful modulation effect and one was unresponsive.

Ultrasound microfluidics confound. In side experiments conducted after this study, we determined that a microfluidics confound was present in the setup. In future experiments, we can completely mitigate this effect by using metal microelectrodes, and there are currently no obvious practical drawbacks or trade-offs to such a substitution. This confound largely undermines any interpretation of this effect in the context of LIFU neuromodulation; the documented effect we describe in Section 3.4.1 is likely to have been a LIFU-induced *chemical* neuromodulation sequence. This hypothesis is supported by the time-course of the modulation effect, which is more consistent with gradual clearance of fluid by the flowing ACSF than any other physical processes.

3.5: Discussion

On replicability. It is unclear why only 57% of rat brain slices were found to be responsive to ultrasound in our setup, especially considering that the presence of the effect was found to be virtually 100% consistent within-slices. Various steps in the method contribute to small amounts of variability between slices, for example: slight variation in orientation of the vibratome cuts, slight variation in position where the electrodes are inserted, and slight variation in position where the slice is located relative to the FUS beam. However, given that the LFPs were intact and similar between all the slices under consideration, it is unlikely that variation in the slicing or electrode insertion accounts for this variability. It is instead possible that an ultrasound intensity beyond the highest level we tested would have elicited a modulation effect in some of the slices that we deemed unresponsive. This possibility would be consistent with our observations about the nature of the effect.

This variation may be accredited to the microfluidics confound that we discovered; the binary successes and failures could then be explained by variation in electrode position causing some slices and not others to be susceptible to the confound. Although the positioning among slices was similar enough to elicit minimal variation in electrical and ultrasonic-pressure conditions, it is feasible that slight differences in positioning could correspond to a greater difference in fluid-dynamic conditions, for example: in one situation, the electrode tip being blocked by tissue, whereas in another slice, the electrode tip being vulnerable to having its KCl dislodged. Other literature in ultrasound research does not report this type of variability, and it is unlikely to arise from any of the physical explanations of ultrasound neuromodulation discussed in Section 1.2 § "Proposed Mechanisms of Ultrasound

Neuromodulation," therefore the fluidics confound is a likely culprit for the highly-binary successes and failures observed in this study.

Sham conditions. The results from the ultrasound-blocking condition account for most forms of unwanted electrical interference between the device and the brain.

We cannot use inferential statistics to compare the success rates on the mesh-pinned basin to the success rates on glass (i.e., to conclude that there is no major effect): the number of experiments in the mesh-pinned basin variant is much lower (4 versus 44); according to the investigator conducting these experiments, the mesh setup is more challenging to properly orient the electrodes in; and brain slices obtained from the same animal do not constitute independent samples. However, obtaining even one successful modulation effect on mesh – and as of October 2021, we had produced the effect in several brain slices – is valuable in suggesting that the presence of a hard substrate is not primarily responsible for the effect.

Our chosen sham conditions, especially the blocking condition, strongly pointed towards an ultrasound-induced effect; however, they could not adequately control for confounding interactions caused by the ultrasound, such as the fluidics confound that was eventually discovered.

3.6: Conclusion

In hippocampal and cortical rat brain slices, we demonstrated that our LIFU pulse sequence interrupts neural signal transmission with near-perfect replicability within-subjects and 57% success rate between-subjects. Unfortunately, this neuromodulation effect is likely to have been dominated by a confounding interaction with the ultrasound, rather than a neuromodulation mechanism endogenous to the tissue. I succeeded in my main goal for the study, which was to validate the novel hardware system within a series of experiments; I was not successful in determining the success rate of modulation effects, because the main effect we observed in the study was primarily mediated by a spurious interaction. Future studies by our groups still benefit from the advancement of these efforts, and we anticipate that after correcting this confound by replacing glass pipette microelectrodes with metal microelectrodes, we can resume our investigations into ultrasound neuromodulation.

4. Conclusion

Summary of Findings and Work

Development of workflow to obtain optimized physical designs for hardware. I took advantage of interfacing between the MATLAB computing environment and the COMSOL Multiphysics specialized simulation environment to produce a series of designs for real-world devices. These designs were customized and optimized according to performance outcomes; additionally, the nature of the multi-objective optimization procedure outputting many viable designs allows for future development staff to choose between them as goals change (without having to re-run design and optimization procedures).

Development of workflow to construct ultrasound devices that are compatible with microscope-bound experiments. The procedures outlined in Chapter 2 of this manuscript (and further detailed in Appendix B "Hardware Developer Manual") – as well as the 3D models provided to future developers (hosted on GitHub at https://github.com/ProteusMRIgHIFU/NFHD_Console) – provide a foundation for new hardware development for similar systems. The control tests we conducted in Chapter 3 likewise provide a guideline to validate future systems.

Successful development of user-friendly system. All the hardware components are modular pieces that are easy to connect and disconnect. The software console manages all necessary calculations as well as instrument setup and control, and automatically generates a log of sonication intensities.

Characterization of a modulation effect in *ex vivo* tissue. Over the course of this thesis, I enabled the characterization of an ultrasound-induced neuromodulation effect in acute brain tissue; however, we later determined that this effect was primarily mediated by an unwanted interaction between the pulsed LIFU and the measurement setup. The degree to which the confound was dominant over any relevant endogenous mechanisms is such that this characterization task is largely invalidated, but the experience gained with the organism and experiment setup do facilitate our continued inquiries.

Future Directions

Re-establishing replicability with the confound corrected. It may be fruitful to advance a study similar to the study described in Chapter 3 after replacing the glass pipette microelectrodes with metal microelectrodes. For any observable effect in brain slices under almost any modality of observation, a similar battery of control tests should be established, and it may also be valuable to determine replicability rates to power more focused and less exploratory studies.

Incorporating other techniques for neuroscientific inquiry. With small modifications to this experiment setup, we can perform calcium imaging and other types of fluorescence imaging to obtain different electrochemical information about the influence of ultrasound, especially any spatial dynamics. Some other viable investigative neuroscience techniques could include the introduction of channel blockers to investigate which categories of ion channels could be responsible for the response to ultrasound. We are also interested in whether there is any ultrasound-induced change to genetic expression, and we can leverage polymerase chain reaction (PCR) or other genetic measurement techniques to investigate this.

Mechanisms studies and studies into effective parameters. Chapter 1 contains an overview of existing hypotheses surrounding LIFU neuromodulation; as of 2021, the current body of evidence does not point conclusively towards any one hypothesis. The task of designing experiments to distinguish the mechanistic frameworks is an undertaking beyond the scope of this document, but the system that I developed should be flexible enough to accommodate those studies and strategies. Inquiries about parameters and mechanisms go hand-in-hand: the setup I developed makes it easy to change any timing parameters and assess the response, and also to change either interrelated intensity parameter (I_{SPPA} or I_{SPTA}) while keeping others the same, which can assist in the task of decoupling those parameters.

References

[1] J. C. Lacefield, “Physics of Ultrasound,” in *Diagnostic Radiology Physics: A Handbook for Teachers and Students*, 2014, pp. 291–309.

[2] K. Lackner, “Chapter 5: The Differential Equations of Flow,” presented at the E4900, Columbia University, 2001. Accessed: Aug. 23, 2021. [Online]. Available: http://www.columbia.edu/itc/ldeo/lackner/E4900/Themelis5.pdf

[3] B. Treeby, B. Cox, and J. Jaros, “k-Wave User Manual,” p. 88, Aug. 2016.

[4] B. O’Leary and S. Vaezy, “Marketing Clearance of Diagnostic Ultrasound Systems and Transducers,” p. 64, Oct. 2017.

[5] F. Ahmadi, I. V. McLoughlin, S. Chauhan, and G. ter-Haar, “Bio-effects and safety of low-intensity, low-frequency ultrasonic exposure,” *Progress in Biophysics and Molecular Biology*, vol. 108, no. 3, pp. 119–138, Apr. 2012, doi: 10.1016/j.pbiomolbio.2012.01.004.

[6] H. H. Pennes, “Analysis of tissue and arterial blood temperatures in the resting human forearm,” *Journal of applied physiology*, vol. 1, no. 2, pp. 93–122, 1948.

[7] P. R. Hoskins, K. Martin, and A. Thrush, Eds., “The British Medical Ultrasound Society. Guidelines for the safe use of diagnostic ultrasound equipment,” in *Diagnostic Ultrasound*, 2nd ed., Cambridge: Cambridge University Press, 2010, pp. 217–225. doi: 10.1017/CBO9780511750885.020.

[8] M. L. Palmeri, A. C. Sharma, R. R. Bouchard, R. W. Nightingale, and K. R. Nightingale, “A finite-element method model of soft tissue response to impulsive acoustic radiation force,” *IEEE Trans. Ultrason., Ferroelect., Freq. Contr.*, vol. 52, no. 10, pp. 1699–1712, Oct. 2005, doi: 10.1109/TUFFC.2005.1561624.

[9] A. Hurrell, “Chapter 5: Transducers,” in *Fundamentals of Medical Ultrasonics*, M. Postema, Ed. Spon Press, 2011, pp. 89–121. doi: 10.1201/9781482266641.

[10] K. Butts Pauly, “Ultrasonic Transducer Fundamentals,” presented at the Rad225 Transcranial Ultrasound Neuromodulation Class 5, Stanford University, 2019. Accessed: Oct. 08, 2021. [Online]. Available: http://web.stanford.edu/class/rad225/subdir/Class5.pdf

[11] F. A. Duck, A. C. Baker, and H. C. Starritt, Eds., *Ultrasound in Medicine*, 1st ed. Boca Raton: CRC Press, 1998. [Online]. Available: https://doi-org.ezproxy.lib.ucalgary.ca/10.1201/9780367802479

[12] G. T. Clement, J. White, and K. Hynynen, “Investigation of a large-area phased array for focused ultrasound surgery through the skull,” *Phys. Med. Biol.*, vol. 45, no. 4, pp. 1071–1083, Apr. 2000, doi: 10.1088/0031-9155/45/4/319.

[13] K. Hynynen *et al.*, “500-element ultrasound phased array system for noninvasive focal surgery of the brain: A preliminary rabbit study with ex vivo human skulls,” *Magnetic Resonance in Medicine*, vol. 52, no. 1, pp. 100–107, Jul. 2004, doi: 10.1002/mrm.20118.

[14] S. W. Flax and M. O’Donnell, “Phase-aberration correction using signals from point reflectors and diffuse scatterers: basic principles,” *IEEE Transactions on Ultrasonics, Ferroelectrics, and Frequency Control*, vol. 35, no. 6, pp. 758–767, Nov. 1988, doi: 10.1109/58.9333.

[15] S. A. Goss, L. A. Frizzell, J. T. Kouzmanoff, J. M. Barich, and J. M. Yang, “Sparse random ultrasound phased array for focal surgery,” *IEEE transactions on ultrasonics, ferroelectrics, and frequency control*, vol. 43, no. 6, pp. 1111–1121, 1996.

[16] M. Akiyama and T. Kamakura, “Elliptically curved acoustic lens for emitting strongly focused finite-amplitude beams: Application of the spheroidal beam equation model to the theoretical prediction,” *Acoust. Sci. & Tech*, vol. 26, no. 3, pp. 279–284, Nov. 2004, doi: https://doi.org/10.1250/ast.26.279.

[17] Y. Kim, A. D. Maxwell, T. L. Hall, Z. Xu, K.-W. Lin, and C. A. Cain, “Rapid prototyping fabrication of focused ultrasound transducers,” *IEEE Trans. Ultrason., Ferroelect., Freq. Contr.*, vol. 61, no. 9, pp. 1559–1574, Sep. 2014, doi: 10.1109/TUFFC.2014.3070.

[18] G. Maimbourg, A. Houdouin, T. Deffieux, M. Tanter, and J.-F. Aubry, “3D-printed adaptive acoustic lens as a disruptive technology for transcranial ultrasound therapy using single-element transducers,” *Phys. Med. Biol.*, vol. 63, no. 2, p. 025026, Jan. 2018, doi: 10.1088/1361-6560/aaa037.

[19] I. Suarez-Castellanos *et al.*, “Ex-Vivo Recording of LEUS-Generated Neural Responses from Mouse Brain Slices Using a Microelectrode Array (MEA) System,” in *2018 IEEE International Ultrasonics Symposium (IUS)*, 2018, pp. 1–4.

[20] J.-W. Lin, F. Yu, W. S. Müller, G. Ehnholm, and Y. Okada, “Focused ultrasound transiently increases membrane conductance in isolated crayfish axon,” *Journal of Neurophysiology*, vol. 121, no. 2, pp. 480–489, Feb. 2019, doi: 10.1152/jn.00541.2018.

[21] P. Langevin, “Procédé et appareils d’émission et de réception des ondes élastiques sous-marines à l’aide des propriétés piézo-électriques du quartz,” FR505703A, Aug. 05, 1920 [Online]. Available: https://patents.google.com/patent/FR505703A/en

[22] R. W. Wood and A. L. Loomis, “The physical and biological effects of high-frequency sound-waves of great intensity,” *The London, Edinburgh, and Dublin Philosophical Magazine and Journal of Science*, vol. 4, no. 22, pp. 417–436, Sep. 1927, doi: 10.1080/14786440908564348.

[23] E. N. Harvey, “THE EFFECT OF HIGH FREQUENCY SOUND WAVES ON HEART MUSCLE AND OTHER IRRITABLE TISSUES,” p. 7, Jul. 1929.

[24] J. G. Lynn, R. L. Zwemer, A. J. Chick, and A. E. Miller, “A NEW METHOD FOR THE GENERATION AND USE OF FOCUSED ULTRASOUND IN EXPERIMENTAL BIOLOGY,” *Journal of General Physiology*, vol. 26, no. 2, pp. 179–193, Nov. 1942, doi: 10.1085/jgp.26.2.179.

[25] K. Hynynen, A. Darkazanli, E. Unger, and J. F. Schenck, “MRI-guided noninvasive ultrasound surgery,” *Medical Physics*, vol. 20, no. 1, pp. 107–115, 1993, doi: 10.1118/1.597093.

[26] S. A. Sapareto and W. C. Dewey, “Thermal dose determination in cancer therapy,” *International Journal of Radiation Oncology*Biology*Physics*, vol. 10, no. 6, pp. 787–800, Apr. 1984, doi: 10.1016/0360-3016(84)90379-1.

[27] J. E. Lingeman, J. A. McAteer, E. Gnessin, and A. P. Evan, “Shock wave lithotripsy: advances in technology and technique,” *Nat Rev Urol*, vol. 6, no. 12, pp. 660–670, Dec. 2009, doi: 10.1038/nrurol.2009.216.

[28] Y.-N. Wang, T. Khokhlova, M. Bailey, J. H. Hwang, and V. Khokhlova, “Histological and Biochemical Analysis of Mechanical and Thermal Bioeffects in Boiling Histotripsy Lesions Induced by High Intensity Focused Ultrasound,” *Ultrasound in Medicine & Biology*, vol. 39, no. 3, pp. 424–438, Mar. 2013, doi: 10.1016/j.ultrasmedbio.2012.10.012.

[29] R. Salomir *et al.*, “Local hyperthermia with MR-guided focused ultrasound: Spiral trajectory of the focal point optimized for temperature uniformity in the target region,” *J. Magn. Reson. Imaging*, vol. 12, no. 4, pp. 571–583, Oct. 2000, doi: 10.1002/1522-2586(200010)12:4<571::AID-JMRI9>3.0.CO;2-2.

[30] R. Salomir, F. C. Vimeux, J. A. de Zwart, N. Grenier, and C. T. W. Moonen, “Hyperthermia by MR-guided focused ultrasound: Accurate temperature control based on fast MRI and a physical model of local energy deposition and heat conduction,” *Magn. Reson. Med.*, vol. 43, no. 3, pp. 342–347, Mar. 2000, doi: 10.1002/(SICI)1522-2594(200003)43:3<342::AID-MRM4>3.0.CO;2-6.

[31] S. K. Calderwood, J. R. Theriault, and J. Gong, “How is the immune response affected by hyperthermia and heat shock proteins?,” *International Journal of Hyperthermia*, vol. 21, no. 8, pp. 713–716, Dec. 2005, doi: 10.1080/02656730500340794.

[32] H.-G. Zhang, K. Mehta, P. Cohen, and C. Guha, "Hyperthermia on immune regulation: A temperature's story," *Cancer Letters*, vol. 271, no. 2, pp. 191–204, Nov. 2008, doi: 10.1016/j.canlet.2008.05.026.

[33] W. J. Fry, J. W. Barnard, F. J. Fry, and J. F. Brennan, "Ultrasounically produced localized selective lesions in the central nervous system," *American Journal of Physical Medicine*, vol. 34, no. 3, pp. 413–23, Jun. 1955.

[34] K. Hynynen *et al.*, "Pre-clinical testing of a phased array ultrasound system for MRI-guided noninvasive surgery of the brain—A primate study," *European Journal of Radiology*, vol. 59, no. 2, pp. 149–156, Aug. 2006, doi: 10.1016/j.ejrad.2006.04.007.

[35] W. J. Elias *et al.*, "A Pilot Study of Focused Ultrasound Thalamotomy for Essential Tremor," *N Engl J Med*, vol. 369, no. 7, pp. 640–648, Aug. 2013, doi: 10.1056/NEJMoa1300962.

[36] W. S. Chang, H. H. Jung, E. J. Kweon, E. Zadicario, I. Rachmilevitch, and J. W. Chang, "Unilateral magnetic resonance guided focused ultrasound thalamotomy for essential tremor: practices and clinicoradiological outcomes," *Journal of Neurology, Neurosurgery & Psychiatry*, vol. 86, no. 3, pp. 257–264, Mar. 2015, doi: 10.1136/jnnp-2014-307642.

[37] L. Bakay, "Ultrasonically Produced Changes in the Blood-Brain Barrier," *Arch NeurPsych*, vol. 76, no. 5, p. 457, Nov. 1956, doi: 10.1001/archneurpsyc.1956.02330290001001.

[38] K. Hynynen, N. McDannold, N. Vykhodtseva, and F. A. Jolesz, "Noninvasive MR Imaging–guided Focal Opening of the Blood-Brain Barrier in Rabbits," *Radiology*, vol. 220, no. 3, pp. 640–646, Sep. 2001, doi: 10.1148/radiol.2202001804.

[39] N. Lipsman *et al.*, "Blood–brain barrier opening in Alzheimer's disease using MR-guided focused ultrasound," *Nat Commun*, vol. 9, no. 1, p. 2336, Dec. 2018, doi: 10.1038/s41467-018-04529-6.

[40] E. S. Krames, P. H. Peckham, A. R. Rezai, and F. Aboelsaad, "Chapter 1: What is Neuromodulation?," in *Neuromodulation*, vol. 1, 2009.

[41] N. A. Mekhail, J. Cheng, S. Narouze, L. Kapural, M. N. Mekhail, and T. Deer, "Clinical Applications of Neurostimulation: Forty Years Later," *Pain Practice*, vol. 10, no. 2, pp. 103–112, Mar. 2010, doi: 10.1111/j.1533-2500.2009.00341.x.

[42] E. L. Simpson, A. Duenas, M. W. Holmes, D. Papaioannou, and J. Chilcott, *Spinal cord stimulation for chronic pain of neuropathic or ischaemic origin: systematic review and economic evaluation*. NIHR Journals Library, 2009. Accessed: Mar. 24, 2019. [Online]. Available: https://www.ncbi.nlm.nih.gov/books/NBK56903/

[43] G. Cruccu *et al.*, "EAN guidelines on central neurostimulation therapy in chronic pain conditions," *European journal of neurology*, vol. 23, no. 10, pp. 1489–1499, 2016.

[44] F. A. Al-Otaibi, C. Hamani, and A. M. Lozano, "Neuromodulation in Epilepsy," *Neurosurgery*, vol. 69, no. 4, pp. 957–979, Oct. 2011, doi: 10.1227/NEU.0b013e31822b30cd.

[45] C. Wu and L. Daggubati, "DBS in Treatment Resistant Depression," *International Neuromodulation Society*, 2013. https://www.neuromodulation.com/dbs-in-treatment-resistant-depression (accessed Mar. 24, 2019).

[46] J. P. O'Reardon *et al.*, "Efficacy and Safety of Transcranial Magnetic Stimulation in the Acute Treatment of Major Depression: A Multisite Randomized Controlled Trial," *Biological Psychiatry*, vol. 62, no. 11, pp. 1208–1216, Dec. 2007, doi: 10.1016/j.biopsych.2007.01.018.

[47] C. Hamani *et al.*, "Deep Brain Stimulation for Obsessive-Compulsive Disorder: Systematic Review and Evidence-Based Guideline Sponsored by the American Society for Stereotactic and Functional Neurosurgery and the Congress of Neurological Surgeons (CNS) and Endorsed by the CNS and American Association of Neurological Surgeons," *Neurosurgery*, vol. 75, no. 4, pp. 327–333, Oct. 2014, doi: 10.1227/NEU.0000000000000499.

[48] T. A. Zesiewicz *et al.*, “Practice Parameter: Treatment of nonmotor symptoms of Parkinson disease: Report of the Quality Standards Subcommittee of the American Academy of Neurology,” *Neurology*, vol. 74, no. 11, pp. 924–931, Mar. 2010, doi: 10.1212/WNL.0b013e3181d55f24.

[49] F. M. Weaver *et al.*, “Bilateral Deep Brain Stimulation vs Best Medical Therapy for Patients With Advanced Parkinson Disease: A Randomized Controlled Trial,” *JAMA*, vol. 301, no. 1, pp. 63–73, Jan. 2009, doi: 10.1001/jama.2008.929.

[50] F. J. Fry, H. W. Ades, and W. J. Fry, “Production of Reversible Changes in the Central Nervous System by Ultrasound,” *Science*, vol. 127, no. 3289, pp. 83–84, Jan. 1958, doi: 10.1126/science.127.3289.83.

[51] H. T. Ballantine, E. Bell, and J. Manlapaz, “Progress and Problems in the Neurological Applications of Focused Ultrasound,” *Journal of Neurosurgery*, vol. 17, no. 5, pp. 858–876, Sep. 1960, doi: 10.3171/jns.1960.17.5.0858.

[52] L. R. Gavrilov, G. V. Gersuni, O. B. Ilyinski, E. M. Tsirulnikov, and E. E. Shchekanov, “A study of reception with the use of focused ultrasound. I. Effects on the skin and deep receptor structures in man,” *Brain Research*, vol. 135, no. 2, pp. 265–277, Oct. 1977, doi: 10.1016/0006-8993(77)91030-7.

[53] L. R. Gavrilov, G. V. Gersuni, O. B. Ilyinsky, E. M. Tsirulnikov, and E. E. Shchekanov, “A study of reception with the use of focused ultrasound. II. Effects on the animal receptor structures,” *Brain Research*, vol. 135, no. 2, pp. 279–285, Oct. 1977, doi: 10.1016/0006-8993(77)91031-9.

[54] L. R. Gavrilov, “Use of focused ultrasound for stimulation of nerve structures,” *Ultrasonics*, vol. 22, no. 3, pp. 132–138, May 1984, doi: 10.1016/0041-624X(84)90008-8.

[55] J. Kubanek, “Neuromodulation with transcranial focused ultrasound,” *Neurosurgical Focus*, vol. 44, no. 2, p. E14, Feb. 2018, doi: 10.3171/2017.11.FOCUS17621.

[56] M. L. Prieto, K. Firouzi, B. T. Khuri-Yakub, and M. Maduke, “Activation of Piezo1 but Not NaV1.2 Channels by Ultrasound at 43 MHz,” *Ultrasound in Medicine & Biology*, vol. 44, no. 6, pp. 1217–1232, Jun. 2018, doi: 10.1016/j.ultrasmedbio.2017.12.020.

[57] J. Kubanek, J. Shi, J. Marsh, D. Chen, C. Deng, and J. Cui, “Ultrasound modulates ion channel currents,” *Scientific Reports*, vol. 6, no. 1, Jul. 2016, doi: 10.1038/srep24170.

[58] D. Liao, F. Li, D. Lu, and P. Zhong, “Activation of Piezo1 mechanosensitive ion channel in HEK293T cells by 30 MHz vertically deployed surface acoustic waves,” *Biochemical and Biophysical Research Communications*, p. S0006291X19315955, Aug. 2019, doi: 10.1016/j.bbrc.2019.08.078.

[59] S.-J. Oh *et al.*, “Ultrasonic Neuromodulation via Astrocytic TRPA1,” *Current Biology*, vol. 29, no. 20, pp. 3386-3401.e8, Oct. 2019, doi: 10.1016/j.cub.2019.08.021.

[60] W. J. Tyler, Y. Tufail, M. Finsterwald, M. L. Tauchmann, E. J. Olson, and C. Majestic, “Remote Excitation of Neuronal Circuits Using Low-Intensity, Low-Frequency Ultrasound,” *PLOS ONE*, vol. 3, no. 10, p. e3511, Oct. 2008, doi: 10.1371/journal.pone.0003511.

[61] Y. Tufail *et al.*, “Transcranial Pulsed Ultrasound Stimulates Intact Brain Circuits,” *Neuron*, vol. 66, no. 5, pp. 681–694, Jun. 2010, doi: 10.1016/j.neuron.2010.05.008.

[62] J. Kubanek, P. Shukla, A. Das, S. A. Baccus, and M. B. Goodman, “Ultrasound Elicits Behavioral Responses through Mechanical Effects on Neurons and Ion Channels in a Simple Nervous System,” *J. Neurosci.*, vol. 38, no. 12, pp. 3081–3091, Mar. 2018, doi: 10.1523/JNEUROSCI.1458-17.2018.

[63] B. Krasovitski, V. Frenkel, S. Shoham, and E. Kimmel, “Intramembrane cavitation as a unifying mechanism for ultrasound-induced bioeffects,” *Proceedings of the National Academy of Sciences*, vol. 108, no. 8, pp. 3258–3263, Feb. 2011, doi: 10.1073/pnas.1015771108.

[64] M. Plaksin, S. Shoham, and E. Kimmel, “Intramembrane Cavitation as a Predictive Bio-Piezoelectric Mechanism for Ultrasonic Brain Stimulation,” *Phys. Rev. X*, vol. 4, no. 1, p. 011004, Jan. 2014, doi: 10.1103/PhysRevX.4.011004.

[65] M. Plaksin, E. Kimmel, and S. Shoham, “Cell-Type-Selective Effects of Intramembrane Cavitation as a Unifying Theoretical Framework for Ultrasonic Neuromodulation,” *eNeuro*, vol. 3, no. 3, Jun. 2016, doi: 10.1523/ENEURO.0136-15.2016.

[66] M. L. Prieto, Ö. Oralkan, B. T. Khuri-Yakub, and M. C. Maduke, “Dynamic Response of Model Lipid Membranes to Ultrasonic Radiation Force,” *PLoS ONE*, vol. 8, no. 10, p. e77115, Oct. 2013, doi: 10.1371/journal.pone.0077115.

[67] M. A. Dinno, M. Dyson, S. R. Young, A. J. Mortimer, J. Hart, and L. A. Crum, “The significance of membrane changes in the safe and effective use of therapeutic and diagnostic ultrasound,” *Phys. Med. Biol.*, vol. 34, no. 11, pp. 1543–1552, Nov. 1989, doi: 10.1088/0031-9155/34/11/003.

[68] W. J. Tyler, “Noninvasive Neuromodulation with Ultrasound? A Continuum Mechanics Hypothesis,” *Neuroscientist*, vol. 17, no. 1, pp. 25–36, Feb. 2011, doi: 10.1177/1073858409348066.

[69] T. Heimburg and A. D. Jackson, “On soliton propagation in biomembranes and nerves,” *Proceedings of the National Academy of Sciences*, vol. 102, no. 28, pp. 9790–9795, Jul. 2005, doi: 10.1073/pnas.0503823102.

[70] A. Jerusalem *et al.*, “Electrophysiological-mechanical coupling in the neuronal membrane and its role in ultrasound neuromodulation and general anaesthesia,” *Acta Biomaterialia*, vol. 97, pp. 116–140, Oct. 2019, doi: 10.1016/j.actbio.2019.07.041.

[71] M. D. Menz *et al.*, “Radiation force as a physical mechanism for ultrasonic neurostimulation of the ex vivo retina,” *J. Neurosci.*, pp. 2394–18, Jun. 2019, doi: 10.1523/JNEUROSCI.2394-18.2019.

[72] K. Yu, X. Niu, E. Krook-Magnuson, and B. He, “Intrinsic functional neuron-type selectivity of transcranial focused ultrasound neuromodulation,” *Nat Commun*, vol. 12, no. 1, p. 2519, Dec. 2021, doi: 10.1038/s41467-021-22743-7.

[73] M. J. Rasch, A. Gretton, Y. Murayama, W. Maass, and N. K. Logothetis, “Inferring Spike Trains From Local Field Potentials,” *Journal of Neurophysiology*, vol. 99, no. 3, pp. 1461–1476, Mar. 2008, doi: 10.1152/jn.00919.2007.

[74] H. Xiong and H. E. Gendelman, Eds., *Current Laboratory Methods in Neuroscience Research*. New York, NY: Springer New York, 2014. doi: 10.1007/978-1-4614-8794-4.

[75] O. Herreras, “Local Field Potentials: Myths and Misunderstandings,” *Front. Neural Circuits*, vol. 10, Dec. 2016, doi: 10.3389/fncir.2016.00101.

[76] K. Tripathi, T. Zhang, N. McDannold, Y.-Z. Zhang, G. Ehnholm, and Y. Okada, “Direct Activation of Cortical Neurons in the Primary Somatosensory Cortex of the Rat in Vivo Using Focused Ultrasound,” *Ultrasound in Medicine & Biology*, vol. 46, no. 9, pp. 2349–2360, Sep. 2020, doi: 10.1016/j.ultrasmedbio.2020.06.003.

[77] I. M. Suarez-Castellanos *et al.*, “Spatio-temporal characterization of causal electrophysiological activity stimulated by single pulse focused ultrasound: an ex vivo study on hippocampal brain slices,” *J. Neural Eng.*, vol. 18, no. 2, p. 026022, Apr. 2021, doi: 10.1088/1741-2552/abdfb1.

[78] P. C. Rinaldi, J. P. Jones, F. Reines, and L. R. Price, “Modification by focused ultrasound pulses of electrically evoked responses from an in vitro hippocampal preparation,” *Brain Research*, vol. 558, no. 1, pp. 36–42, Aug. 1991, doi: 10.1016/0006-8993(91)90711-4.

[79] M. R. Bachtold, P. C. Rinaldi, J. P. Jones, F. Reines, and L. R. Price, “Focused Ultrasound Modifications of Neural Circuit Activity in a Mammalian Brain,” *Ultrasound in Medicine & Biology*, vol. 24, no. 4, pp. 557–565, May 1998, doi: 10.1016/S0301-5629(98)00014-3.

[80] R. F. Dallapiazza *et al.*, “Noninvasive neuromodulation and thalamic mapping with low-intensity focused ultrasound,” *Journal of Neurosurgery*, vol. 128, no. 3, pp. 875–884, Mar. 2018, doi: 10.3171/2016.11.JNS16976.

[81] M. Hayner and K. Hynynen, “Numerical analysis of ultrasonic transmission and absorption of oblique plane waves through the human skull,” *The Journal of the Acoustical Society of America*, vol. 110, no. 6, pp. 3319–3330, Dec. 2001, doi: 10.1121/1.1410964.

[82] P. J. White, G. T. Clement, and K. Hynynen, “Local frequency dependence in transcranial ultrasound transmission,” *Phys Med Biol*, vol. 51, no. 9, pp. 2293–2305, May 2006, doi: 10.1088/0031-9155/51/9/013.

[83] R. L. King, J. R. Brown, W. T. Newsome, and K. B. Pauly, “Effective Parameters for Ultrasound-Induced In Vivo Neurostimulation,” *Ultrasound in Medicine & Biology*, vol. 39, no. 2, pp. 312–331, Feb. 2013, doi: 10.1016/j.ultrasmedbio.2012.09.009.

[84] N. Andreasson, A. Evgrafov, and M. Patriksson, “An Introduction to Optimization: Foundations and Fundamental Algorithms,” p. 348, 2005.

[85] H. B. Curry, “The method of steepest descent for non-linear minimization problems,” *Quart. Appl. Math.*, vol. 2, no. 3, pp. 258–261, Oct. 1944, doi: 10.1090/qam/10667.

[86] K. Levenberg, “A method for the solution of certain non-linear problems in least squares,” *Quart. Appl. Math.*, vol. 2, no. 2, pp. 164–168, Jul. 1944, doi: 10.1090/qam/10666.

[87] L. Liberti, “Introduction to Global Optimization,” *École Polytechnique*, p. 43, Oct. 2008.

[88] F.-S. Wang and L.-H. Chen, “Heuristic Optimization,” in *Encyclopedia of Systems Biology*, W. Dubitzky, O. Wolkenhauer, K.-H. Cho, and H. Yokota, Eds. New York, NY: Springer New York, 2013, pp. 885–885. doi: 10.1007/978-1-4419-9863-7_411.

[89] H. Kim, S. D. Lee, A. Chiu, S.-S. Yoo, and S. Park, “Estimation of the spatial profile of neuromodulation and the temporal latency in motor responses induced by focused ultrasound brain stimulation,” *NeuroReport*, vol. 25, no. 7, pp. 475–479, May 2014, doi: 10.1097/WNR.0000000000000118.

[90] H.-C. Kim *et al.*, “Transcranial focused ultrasound modulates cortical and thalamic motor activity in awake sheep,” *Sci Rep*, vol. 11, no. 1, p. 19274, Dec. 2021, doi: 10.1038/s41598-021-98920-x.

[91] H. F. Stewart, “Ultrasonic Measurement Techniques and Equipment Output Levels,” in *Essentials of Medical Ultrasound: A Practical Introduction to the Principles, Techniques, and Biomedical Applications*, M. H. Repacholi and D. A. Benwell, Eds. Springer Science & Business Media, 2012, pp. 77–111.

[92] J. D. Sweatt, Ed., “Long-Term Potentiation — A Candidate Cellular Mechanism for Information Storage in the Central Nervous System,” in *Mechanisms of Memory*, 2nd ed., Academic Press, 2009, pp. 151–190.

Appendix A: System User Manual

User Manual: **NFHD USBEAM** (**U**ltrasound **S**ystem for **B**rain **E**xperiments under **A** **M**icroscope)

Last Updated Jan 18, 2022 — Jak Loree-Spacek

Preamble: The NFHD Ultrasound System for Brain Experiments under Microscope comprises 5 physical units: a transducer unit (assigned its own model number of the form NFHD-0XX); an electrical matching box that is associated with the particular transducer unit (assigned a model number of the form NFHD-0XXM); a resin-printed basin for mounting the transducer unit and the sample; the aluminum stage that is fixed to the microscope and the microscope table; and an FDM-printed adapter to couple the basin with the metal stage. Auxiliary to this system are an electrical source with output resistance 50 Ω (frequently a function generator plus RF amplifier) and the software "NFHD Console." This document describes the assembly and usage of these parts in preparation for their application in brain experiments.

Section 1: Figures and Schematics Describing the Basin System

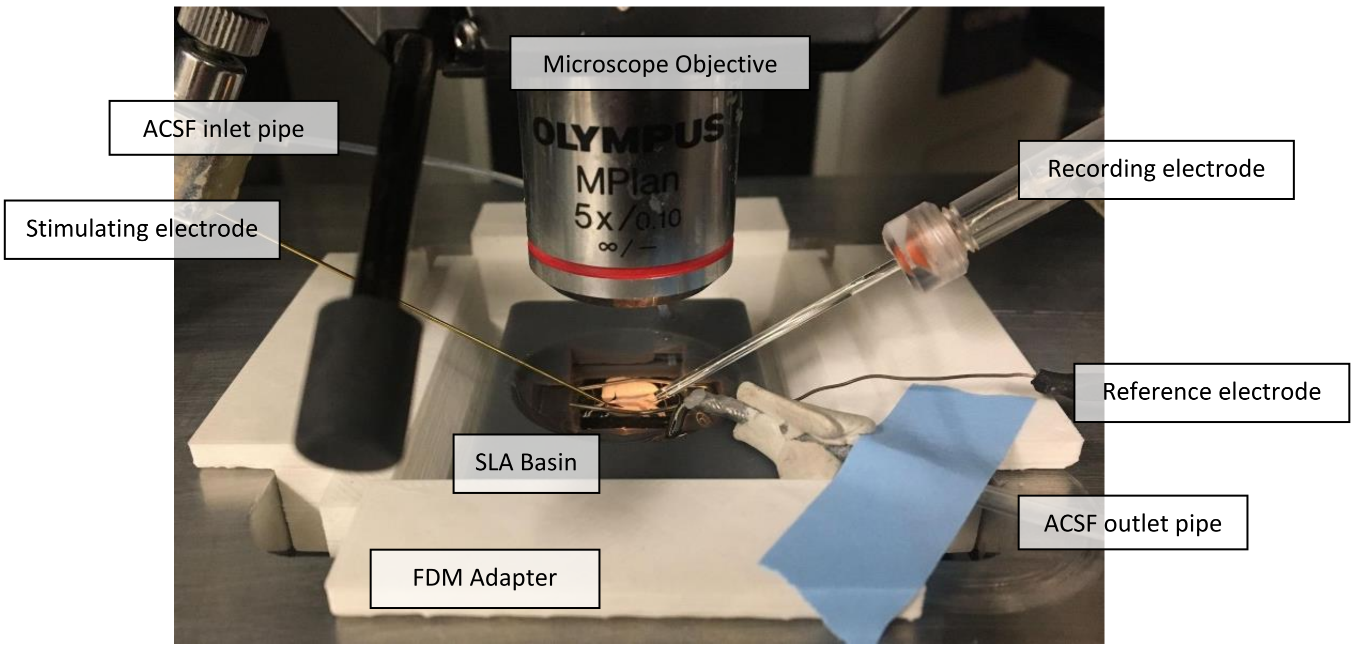

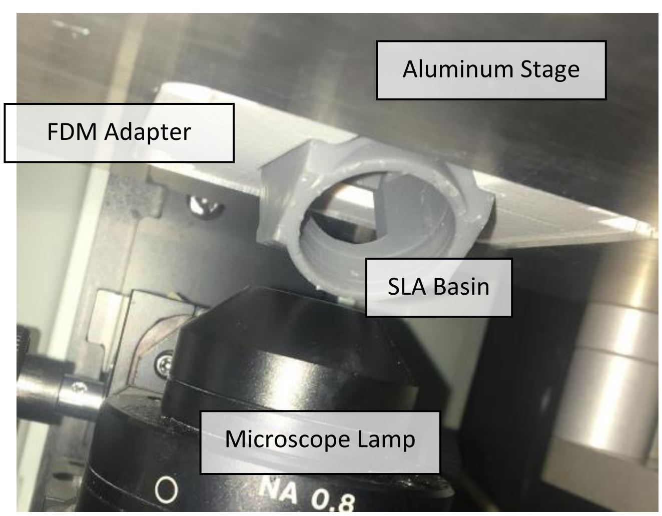

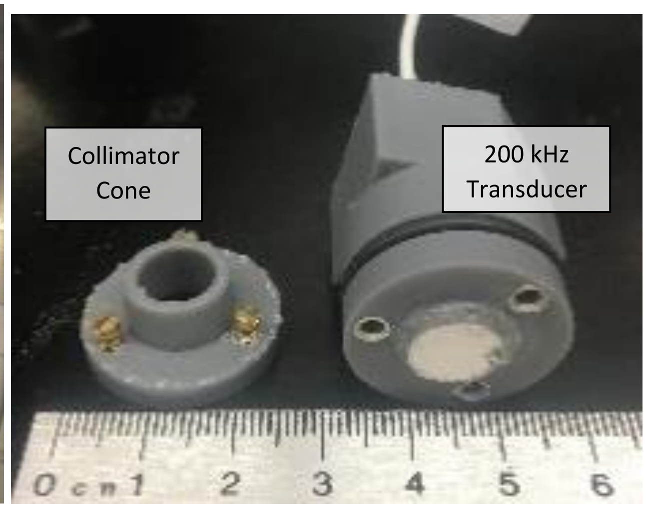

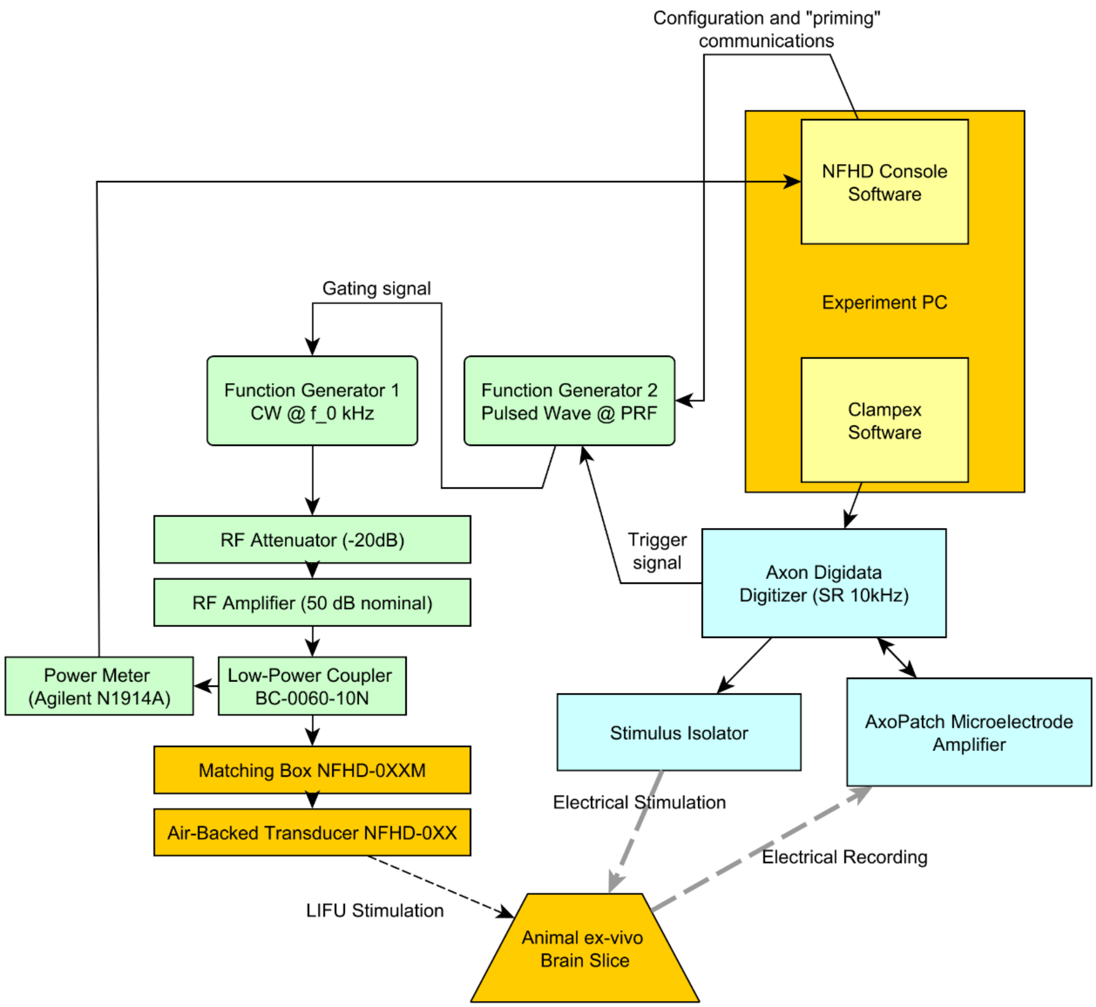

<u>Section 2:</u> Typical Operating Procedure

1. Assemble all the static elements (metal platform, plastic adapter, and resin basin) within the microscope setup. Ensure the basin is clean and free of dirt and residues.
2. Check integrity of the transducer unit:
   a. Brass screws tightly join the bottom and top components;
   b. Silicone seal appears intact;
   c. Insulating tape on transducer surface has not come loose or detached.
3. Insert the transducer into the main aperture of the basin. The circular indentations correspond to the nitrile O-ring on the shaft of the transducer. As of the most recent hardware revision, the *forward position* corresponds to the beam targeting circles drawn on the glass mounting slide.
4. Connect the electronic parts:
   a. Connect the tail of the transducer to its associated matching box (for example, the unit labelled NFHD-014 should be connected to the matching box labelled NFHD-014M) using an MCX to BNC adapter. An arrow is marked on the matching box to indicate which port connects to the transducer, as “TX→ ”.
   b. Connect the remaining port of the matching box to the amplifier using a 50 Ω coaxial cable with BNC terminations.

   i. Whichever electrical stimulus source is chosen (i.e. whichever amplifier is used), there should be a characterization YAML file that is specific to the transducer *and* to the amplifier.
   ii. As of the most current hardware revision, all the configuration YAML files are specific to the big blue broadband amplifier.

c. Connect the function generator to a computer with NI-VISA drivers and the NFHD Control Console installed. Use a USB-B connector (a "printer cable" or "serial cable").
   i. Go to https://www.ni.com/en-ca/support/downloads/drivers/download.ni-visa.html to download and install necessary drivers. For research computers that must remain disconnected from the Internet, an offline copy of the driver installation image is available from the same page, which may be downloaded to a portable media drive and mounted to the offline computer.
   ii. Instructions for installing and running the NFHD Control Console are included in the application's README file. The computer should have an installation of Anaconda Python (also installable offline via portable media drive).

d. With BNC cables, install a low-power coupler and power meter between the amplifier and the matching box. Connect the power meter to the same lab computer as in (c) via USB-to-RS232 cable.
   i. The current calibration system does not need the power meter feedback, but it may be useful for automated data logging, especially if you decide to sonicate outside the canonical calibration range.
   ii. *Developer note:* Even though the power meter feedback is not necessary for the protocol anymore, as of software revision 1.1, the NFHD Console still relies on connecting and communicating with the Power Meter within its workflow.

5. Insert ACSF circulation tubes into the resin basin. The inlet tube has a built-in channel to help hold it in place; the outlet tube may be held in position with reusable putty adhesive. ACSF may be circulated at this point.
   a. Check the integrity of waterproof seal(s) before proceeding with the brain electrophysiology experiment protocol. If the main seal between the basin and the transducer appears leaky, the O-ring may not be aligned properly with its indentation. If the seal between the glass slide and the basin appears leaky, this may be quickly rectified with petroleum jelly as a short-term solution (with no cure time needed), or alternatively with windshield silicone as a longer-term solution (up to 24h cure time usually needed).
6. The brain slice may be positioned on the glass slide at this point. Two circular contours are traced onto the glass slide. With respect to *pressure*, the inner contour corresponds to 70.8% of maximum and the outer contour corresponds to 49.8% of maximum (3 dB down and 6 dB down respectively). With respect to *intensity*, the inner contour corresponds to 49.8% of maximum.
7. When sonication is desired, the NFHD Control Console can be used to send the calculated parameters directly to the function generator, and then subsequently to perform a simple timed exposure.
   a. Reminder: the calculated parameters output by the Console are only accurate for a particular transducer AND amplifier. The selected YAML file contains an entry confirming which amplifier was used to generate calibration data.

Appendix B: NFHD Developer Manual

Jak Loree-Spacek

Last updated January 2022

1. **Printing backing unit, basin, cone with resin stereolithography**
    a. Obtain the STL file(s) from github.com/ProteusMRIgHIFU/NFHD_Console
    b. (If you need a new adapter, print the adapter on FDM rather than SLA printer to save material. Precision is not important for that component.)
    c. Check the revision number in the filename. Backing unit should be backing_inserts_v40
        i. Cone is cone_inserts_vented_v24
        ii. Adapter is adapter_threaded_v5
        iii. Basin is basin_glass_v39 OR basin_mesh_v4
    d. Before commencing a print, it is recommended to read available instructional material from support.formlabs.com: recommended material includes articles entitled "Printing with the Form 3," "Maintaining the Form 3," "Troubleshooting the Form 3," and "Finishing SLA prints"
        i. Similarly, consult the Formlabs support webpages in case of print failures and error messages
    e. If you are using a personal computer, add the Form 3 via IP address. (Retrieve the IP address from the printer in-person.)
        i. You need to either be connected to the UCalgary network *OR* VPN'd into the UCalgary network to be able to see the printer.
    f. In PreForm, position models with the pentagonal face of the backing component towards the build plate, with the aperture face of the basin component towards the build plate, and with the wider circle of the collimator component towards the build plate. Generate supports (default settings are OK).
        i. They are oriented this way to ensure slight miscalibrations in the Z-axis don't interfere with the circular parts that must interface. In short, print anything that must be circular in the X-Y plane, which is parallel with the build plate.
        ii. If PreForm tells you there is an incompatibility between firmware versions, do NOT update the printer; use the desktop PC in Dr. Curiel's lab (where the Form 3 is currently located).
    g. Commence the print. You can start it remotely if the printer was "Primed," or you can send the file over the network and then start the print in-person via the controls on the printer.
        i. You need to either be connected to the UCalgary network *OR* VPN'd into the UCalgary network to be able to submit the print file.
    h. Finish the print: put gloves on both hands. Carefully remove the build plate from the machine (lift the locking lever and slide the plate towards yourself); snap the print off the build plate.
        i. Inspect it for any printing faults (faults seem to be more common with the black resin than the gray resin).
        ii. Remove the supports with side-cutters, and place the part in the Form Wash to remove most of the uncured resin.
        iii. ***Additional steps for finishing the cones:*** Fill a squirt-bottle with isopropyl alcohol (99% preferred). Use the thin nozzle on the squirt-bottle to push IPA through the eight vent holes on the cone. Hold the cone up to the light to verify that it is cleared of uncured resin. Then, using a small paintbrush, apply a very small amount of the resin to cover 7 of the 8 holes (doesn't matter which 7). (The final hole must stay open for the curing to let air escape; seal it later with silicone.)
        iv. Put the piece(s) into the Form Cure machine at 45-60 degrees C for 30-90 minutes.
    i. Post-finishing:
        i. Add three threaded inserts (4-40 thread, length code 1) and a nitrile O-ring (11/16" ID, 7/8" OD, 3/32" thick) to the transducer backing. For the basin components: Cut a 25mm x 1mm x 75mm

glass slide into a segment that covers the optical window on the bottom and a segment that will slide into the main chamber. (To cut glass slide, score the glass with a knife and then carefully crack it on an uneven surface.) Use contact cement (e.g. Gorilla Glue) to adhere the optical window. The main chamber slide should pressure-fit adequately, but you can optionally use contact cement if it is loose. If necessary, use petroleum jelly to waterproof the glass slide slot.

ii. For the mesh-pinned variant of the basin design, use a craft or clothing fabric and fix it with the shafts of brass tacks.

2. **Assembling transducer into backing.**
   a. Necessary materials: 1x backing; 1x transducer with 200 kHz nominal fundamental frequency, d = 10mm; 1x pre-crimped coaxial cable with BNC or MCX connector, cable type RG-178; flowable windshield silicone (word “flowable” on packaging seems important); SciGrip 16 or similar fast-setting acrylic cement; solder, digital temperature control soldering iron, solder flux; heat shrink wrap; craft knife or scalpel; “MMCX” super thin coaxial cable; heat gun.
   b. Cut two segments of micro-micro coaxial cable -- one to ~2cm and one to ~3cm. With a scalpel, shave the outer insulation off of the cable to expose the shielding/ground; then, peel away the ground braid with your fingers.
      i. Use the scalpel again to shave off the insulation protecting the “hot” conductor, approx. 0.5cm on each end of each segment of wire. Do this by placing the wire against the cutting board and scraping the blade near-perpendicular to the board surface, as though peeling a vegetable.
      ii. Flux and tin each end of these connector wires.
   c. Cut the pre-crimped cable in half to produce two wire assemblies, each with a crimped connector on one side and exposed coaxial cable on the other.
      i. Feed the exposed end through the bottom of the resin-printed transducer backing. Add a short (~0.4cm long) segment of heat-shrink wrap to the exposed end and use a heat gun to fix it in place. (This segment helps protect against pulling backwards on the wire.)

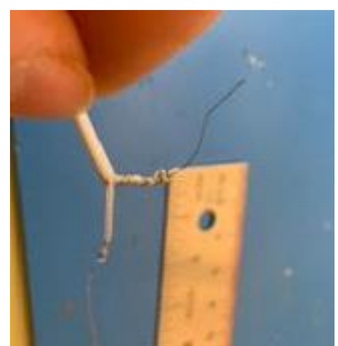

      ii. Strip the exposed end 1 cm of its outermost insulation. Separate the braided “ground” from the insulated “hot” inside. One useful technique is to enlarge a hole in the side of the round braid, and pull the central conductor out through this hole. Pull the two separated conductors away from each other as though a “Y” shape; each leg of the Y-shape should be no more than 6 mm long. Strip the tip of the “hot” wire 2 mm, and tin and flux both conductors.

      iii. Flux the front and back surfaces of the transducer where the wires will connect. (For the top, as close to the circumference as possible; for the bottom, close to the center of the crystal.) With the soldering iron set to 710 degrees F, solder the connector wires to the transducer (the longer one to the front surface, the shorter one to the back surface). **Do not use traditional soldering technique; use less than a drop of high-gauge solder, melt it onto the iron, and briefly touch the iron to the wire and electrode. Practice this technique copiously on spare transducers to get experience making the solder blob as small as possible.

iv. Prepare two segments of heat-shrink wrap just long enough to protect the connectors from touching one another near the base of the casing. Slide them over the wire segments, then solder the back wire to the ground of the coax, and solder the front wire to the hot of the coax. Position and shrink the heat-shrink wrap.

**The order of assembly (i.e. [solder to the coax, then the transducer] versus [solder to the transducer, then the coax) does not matter much. I think most people who have done this assembly prefer the former order.*

d. Carefully retract the assembly into the resin transducer backing. Ensure the front connector wire goes through the dedicated thin channel in the backing (i.e. that is it not pinched underneath the transducer).

i. Pinch the bottom cable with an alligator-style clip at the workbench. Using a paintbrush or similar application aid, apply a layer of flowable windshield silicone between the top of the transducer surface and the edge of the casing. See image to the immediate right for example of adequate waterproofing.

ii. Do not aim to fill the space between the transducer and the casing, just waterproof the top surface. Also be careful not to spill much silicone onto the rim of the casing; the cone needs to screw on flush.

iii. Wait 24h for the silicone to cure.

iv. Invert the device within the workbench clip (so the transducer faces down). Using a paintbrush or similar application aid, apply a layer of SciGrip 16 or similar acrylic cement compound to the interface between the back face of the casing & the coaxial cable. This serves to both (1) mechanically fix the wire to the casing to protect against pulling, pushing, and rotation, and (2) waterproof the same interface. See image to the right for example of adequate cementing.

v. Wait 24h for cement to cure.

e. Add polyimide tape to the front (exposed) surface of the transducer. One convenient technique to deal with the vertical displacement of the solder blob is to cover most of the surface but not the solder blob with one piece of tape, and use a second piece to cover the rest. (See the two images to the right.)

3. **Matching.** Using a Vector Network Analyzer (VNA) and a water bath, construct a matching box for the transducer. Document the device's natural resonance

pre-match and the position of minimum reflection post-match. (For example, the nominal resonant frequency will be 200.0 kHz, the natural resonance pre-match may be 192.5 kHz, and then after matching the VNA may show that minimum reflection occurs at 193.5 kHz due to tolerances, parasitics, etc.)

a. Useful websites that may assist in matching box calculation/construction: https://www.qsl.net/in3otd/parallr.html <= if you need a target capacitance, this can help you compute how to get as close as possible using common discrete component values https://home.sandiego.edu/~ekim/e194rfs01/jwmatcher/matcher2.html <= cheat sheet for matching circuit calculation at a target frequency. Convenient architecture for us is Low-pass "low-high" network (inductor in series, capacitor in parallel). N.B.: The author of this manual has not actually experimented with other network configurations.
b. Secure your device in the water bath before you begin. Small amounts of wiggling in the setup will make it very frustrating to obtain consistent measurements.
c. Connect the VNA to the transducer. Make sure it is calibrated in the plane of the transducer connector port (this means, don't use default/factory calibration settings! Use the cal kit at the end of the coaxial cable length you are using and/or "fixture length compensation" to ensure you are looking at the correct electrical plane).
d. Set the VNA frequency scan range to 150kHz-250kHz, 1000 points resolution (i.e. 200 Hz step). Find the resonance frequency using a reflection mode (SWR, for example) and minimum-search with a marker. Switch to Smith Chart format to obtain real and imaginary impedance at that frequency. Use the above "cheating" website to design a matching circuit that transforms your recorded complex impedance to 50+j0 Ω at your selected frequency. (Don't forget you can use the VNA to check component capacitance/inductance values more precisely than their labels.)
e. Construct the box, connect everything, and record your operating frequency and the SWR at that frequency. The SWR will predict what ratio of electrical power is reflected back from the circuit (and into the driving amplifier).
    i. Do not assume that this ratio is preserved across all power levels! Testing has revealed that impedance can change significantly with delivered power (due to heating or clamping effects, or possibly something else like magnetic saturation). If you are going to sonicate at significant delivered power (more than 200 mW), use a dual-directional coupler and power meter to verify what portion of power will be reflected, and check against amplifier spec sheets what the amplifier can tolerate.

4. Characterization: Acoustic Field Intensity and Shape.

a. A calibrated hydrophone is the current preferred method of characterizing the acoustic field. It is both more precise and more convenient.
    i. If a calibrated hydrophone is not available, the *radiation force method* can be used to approximate acoustic conversion efficiency [and then the pressure-voltage conversion for your working frequency] via a procedure outlined in the documents of Dr. Pichardo ("Recover pressure values.docx," 2019).
b. Fill the acoustic tank with degassed and deionized water. Degas it again once filled for >45min.
c. For free-field or to verify the field at the aperture of the collimator cone, the pentagonal shape of the backing fits within the screw-clamps that can be found in both the EIC acoustic tank and the USTLab acoustic tank. To instead generate a calibration file for the microscope experiments, first install the transducer in the desired basin in the desired position (either forward or retracted slot); then, mount the basin into the screw-clamp such that the basin is pinched below its overhangs, and the top surface of the

basin is parallel with the body of the clamp. In this configuration, the transducer will be ~40 degrees angle to the needle hydrophone.

d. Install the needle hydrophone into a holder on the three-axis positioning system. Consult the documentation to see whether the hydrophone needs pre-amplification before being connected to an oscilloscope. (The ONDA 0.5mm calibrated hydrophone, for example, does not – it is connected directly to a high-Z input on scope.) Move the hydrophone as close as safely possible to the glass slide within the basin. Set the safety limits of the 3D positioning system accordingly.
e. Power the transducer. It is recommended to use an RF amplifier (and to record which amplifier is used) for the sake of acquiring end-to-end calibration data (that is to say: so that you may obtain a calibration curve that goes directly from function generator volts → peak acoustic pressure in kPa, without relying on intermediate measures), HOWEVER be sure to use a small duty cycle (2% or less) on the function generator; this is for the protection of the needle hydrophone.
    i. When choosing number of pulses and duty cycle, ensure you have enough pulses for the pressure to reach steady-state.
f. Configure the oscilloscope to have a moderate number of acquiring averages (~8), so that a planar scan does not smear values. Using the MATLAB interface to the 3D positioner, perform a Planar Scan with dimensions 2mm x 2mm and step size 1mm; this will help locate the "spatial peak" of pressure. Use visual identification to ensure your spatial peak is still over top of the glass, i.e. where the brain slice can actually sit. In testing, it has been determined that pressure is slightly higher off the glass, and spatial-peak will likely be right on the edge.
g. Set the number of averages higher (~50 for the ONDA hydrophone, which has a lot of wiggle). Choose a lower and upper bound of input voltages to test, and choose values in-between; the author of this manual appreciates geometrically-spaced values rather than linearly-spaced (in Python, `numpy.geomspace(min,max,points)`). For each stimulus, record the peak deviation in voltage, and convert it to peak pressure in Pa or kPa.
    i. It is slightly more precise to use serial communications to obtain the waveform from the scope, select an interval of steady-state pressure
    ii. Don't forget to randomize order. An easy way to do this is random.org/lists/.
    Similarly, consider taking 2 or 3 repetitions.
    iii. Keep an eye out for unusual effects at high power, for example: transients that are higher-amplitude than anticipated, or severe deviations in impedance that lead to significant energy reflection back into the amplifier. (To capture this latter effect, it is usually prudent to use a power meter during these tests, even if you are not primarily looking to record power delivery as part of characterization.) These should be recorded, and the `cal_range` field in the finished .yaml file should only cover the "safe"/"predictable"/"canonical" calibration range.
h. Generate the .yaml file for this transducer. Include the following fields:
    i. Transducer's unit name and operating frequency (`name, frequency`)
    ii. Information about the calibration data collection: Amplifier and hydrophone used, date of collection, and optionally there is room to add any notes about acquisition & where to find the raw data files. (`amplifier, hydrophone, acquisition_notes`)
    iii. Calibration range and calibration data: a two-element min and max calibration range; a custom message to warn the user what may happen when they go out-of-range; and two vectors corresponding to the input mV and the output Pascals at spatial-peak. (`cal_range, out_of_cal_message, mV, and Ppeak`)